KINEMATICS OF 10 EARLY-TYPE GALAXIES FROM *HUBBLE SPACE TELESCOPE* AND GROUND-BASED SPECTROSCOPY[1]

JASON PINKNEY,[2,3] KARL GEBHARDT,[4] RALF BENDER,[5] GARY BOWER,[6] ALAN DRESSLER,[7] S. M. FABER,[8]
ALEXEI V. FILIPPENKO,[9] RICHARD GREEN,[10] LUIS C. HO,[7] JOHN KORMENDY,[4] TOD R. LAUER,[10]
JOHN MAGORRIAN,[11] DOUGLAS RICHSTONE,[2] AND SCOTT TREMAINE[12]

ABSTRACT

We present stellar kinematics for a sample of 10 early-type galaxies observed using the Space Telescope Imaging Spectrograph (STIS) aboard the *Hubble Space Telescope* and the Modular Spectrograph on the MDM Observatory 2.4 m telescope. These observations are a part of an ongoing program to understand the coevolution of supermassive black holes and their host galaxies. Our spectral ranges include either the calcium triplet absorption lines at 8498, 8542, and 8662 Å or the Mg *b* absorption at 5175 Å. The lines are used to derive line-of-sight velocity distributions (LOSVDs) of the stars using a maximum penalized likelihood method. We use Gauss-Hermite polynomials to parameterize the LOSVDs and find predominantly negative h4 values (boxy distributions) in the central regions of our galaxies. One galaxy, NGC 4697, has significantly positive central h4 (high tail weight). The majority of galaxies have a central velocity dispersion excess in the STIS kinematics over ground-based velocity dispersions. The galaxies with the strongest rotational support, as quantified with v_{max}/σ_{STIS}, have the smallest dispersion excess at STIS resolution. The best-fitting, general, axisymmetric dynamical models (described in a companion paper) require black holes in all cases, with masses ranging from $10^{6.5}$ to $10^{9.3}$ $M_\odot$. We replot these updated masses on the M_{BH}-σ relation and show that the fit to only these 10 galaxies has a slope consistent with the fits to larger samples. The greatest outlier is NGC 2778, a dwarf elliptical with relatively poorly constrained black hole mass. The two best candidates for pseudobulges, NGC 3384 and NGC 7457, do not deviate significantly from the established relation between M_{BH} and σ. Neither do the three galaxies that show the most evidence of a recent merger, NGC 3608, NGC 4473, and NGC 4697.

Subject headings: galaxies: elliptical and lenticular, cD — galaxies: kinematics and dynamics

On-line material: color figures, machine-readable tables

1. INTRODUCTION

The wealth of new data from the Space Telescope Imaging Spectrograph (STIS) aboard the *Hubble Space Telescope* (*HST*) is dramatically improving our understanding of the central regions of early-type galaxies. Its long-slit design allows for more efficient measurement of galaxy kinematics than the previous Faint Object Spectrograph. The $\sim0\farcs1$ spatial resolution of STIS resolves the influence of a 10^8 $M_\odot$ black hole (BH) in an $L*$ galaxy (velocity dispersion $\sigma = 200$ km s^{-1}) out to ~25 Mpc.

Our team has observed a sample of 10 nearby elliptical or lenticular galaxies using STIS in order to address many questions concerning the demographics of supermassive black holes: Are BHs present in the centers of all early-type galaxies? With which properties of the host galaxy does the BH mass correlate? What can this tell us about the evolution of BHs and galaxies and the relationship of inactive BHs in nearby galaxies to more distant active galactic nuclei (AGNs)? Our data can also address several issues in the evolution of galaxies. For example, why is there a dichotomy between power-law and core surface brightness profiles (Faber et al. 1997)? Were cores created by the scouring action of merging black holes? Why do a few elliptical galaxies not fit well into either category (Rest et al. 2001)? Why are the properties of BHs in bulges and *pseudobulges* so similar, when these two types of stellar systems probably formed in quite different ways (Kormendy et al. 2003)? Our

[2] Department of Astronomy, University of Michigan, 500 Church Street, Ann Arbor, MI 48109; jpinkney@astro.lsa.umich.edu, dor@astro.lsaumich.edu.

[3] Department of Physics and Astronomy, Ohio Northern University, Ada, OH 45810; j-pinkney@onu.edu.

[4] Department of Astronomy, University of Texas at Austin, RLM 15.308, Austin, TX 78712; gebhardt@astro.as.utexas.edu, kormendy@astro.as.utexas.edu.

[5] Universitäts-Sternwarte, Scheinerstrasse, München 81679, Germany; bender@usm.uni-muenchen.de.

[6] Computer Sciences Corporation, Space Telescope Science Institute, 3700 San Martin Drive, Baltimore, MD 21218; bower@stsci.edu.

[7] Carnegie Observatories, Carnegie Institution of Washington, 813 Santa Barbara Street, Pasadena, CA 91101; dressler@ociw.edu, lho@ociw.edu.

[8] University of California Observatories, Lick Observatory, University of California at Santa Cruz, Santa Cruz, CA 95064; faber@ucolick.org.

[9] Department of Astronomy, University of California at Berkeley, 601 Campbell Hall 3411, Berkeley, CA 94720-3411; alex@astro.berkeley.edu.

[10] Kitt Peak National Observatory, National Optical Astronomy Observatory, P.O. Box 26732, Tucson, AZ 85726; green@noao.edu, lauer@noao.edu.

[11] University of Durham, Science Laboratories, South Road, Durham DH1 3LE, England, UK; john.magorrian@durham.ac.uk.

[12] Princeton University Observatory, Peyton Hall, Princeton, NJ 08544; tremaine@astro.princeton.edu.

sample contains galaxies with both core and power-law profiles. It also contains two possible pseudobulges: the low-luminosity S0 NGC 7457 and the S0 NGC 3384.

The data set presented in this paper has already been instrumental in establishing a new, fundamental correlation between the BH mass and stellar velocity dispersion (M_{BH}-σ; Gebhardt et al. 2000, hereafter G00; Ferrarese & Merritt 2000). By combining our data with other published results, G00 demonstrate that the new correlation has less scatter than the one between BH mass and bulge luminosity (see Kormendy & Richstone 1995; Magorrian et al. 1998; Richstone et al. 1998; van der Marel & van den Bosch 1998). Here we give the details of data reduction leading to this result. In a companion paper (Gebhardt et al. 2003) we discuss the modeling technique used to determine the BH masses, while Tremaine et al. (2002) discuss the slope of the M_{BH}-σ relation.

The present paper complements the modeling paper by parameterizing the stellar line-of-sight velocity distributions (LOSVDs) with a Gauss-Hermite (GH) expansion. The parameterization of LOSVDs with GH polynomials has become common practice over the last decade as increasing importance has been placed on the precise shape of the stellar LOSVD (van der Marel & Franx 1993; Bender, Saglia, & Gerhard 1994, hereafter BSG94). High-quality galaxy spectra have demonstrated that stellar LOSVDs deviate significantly from a Gaussian distribution (Bender 1990; Gerhard 1993; van der Marel & Franx 1993). For edge-on, rapidly rotating galaxies, the LOSVD is often asymmetric. In other cases it has longer or shorter tails compared to a Gaussian. In the GH expansion, the first term measures the mean velocity and velocity dispersion, the second term measures asymmetric deviations from a Gaussian, while the third term measures symmetric deviations from a Gaussian. Measuring the entire LOSVD, rather than just its first two moments (mean velocity and velocity dispersion), constrains the phase-space distribution of the stars and thus helps to reduce the ambiguities in the mass distribution derived from stellar kinematics. Although the fully general LOSVD is used in our BH modeling, the GH parameters are a convenient means of describing an LOSVD. They provide a check on the orbital anisotropies determined by the modeling and a means of comparison to previously published results.

The GH parameters can also be combined with photometric and kinematic parameters to provide insight into elliptical galaxies. For example, BSG94 define mean parameters $\langle h_3 \rangle$ and $\langle h_4 \rangle$ and find correlations between these and a_4/a, v/σ, M_B, and v/σ^* for 44 elliptical galaxies. The greater generality of the GH parameterization has been exploited in deriving mass profiles from ground-based spectroscopy for NGC 4342 (Cretton & van den Bosch 1999), NGC 3115 (Emsellem, Dejonghe, & Bacon 1999), NGC 1399 (Saglia et al. 2000), NGC 2974 (Cinzano & van der Marel 1994), and NGC 2434 (Rix et al. 1997). In the case of M87, ground-based GH parameters have even been used to constrain the mass of the central BH (van der Marel 1994b). Many papers present GH parameters derived from ground-based spectroscopy for large samples of galaxies (e.g., Kaprolin & Zeilinger 2000; Kronawitter et al. 2000; Fisher 1997). Checks and comparisons to our ground-based GH parameters come largely from the samples of BSG94 and Halliday et al. (2001), which have five and three galaxies in common, respectively. STIS now enables us to examine the

GH parameters at subarcsecond resolution. For NGC 1023 (Bower et al. 2001) and M32 (Joseph et al. 2001), STIS has clearly revealed the influence of a BH on the stars.

This paper proceeds as follows. We describe our galaxy sample in § 2 and the observations in § 3. Section 4 details the reduction of STIS and complementary ground-based data. In § 5 we first describe how LOSVDs and GH parameters are derived from our spectra, and then we present our kinematics for individual galaxies. In § 6 we discuss our results.

2. SAMPLE DESCRIPTION

A collage of all 10 target galaxies is shown in Figure 1 and Table 1 lists some of their basic properties. The galaxies were chosen from those with reliable surface brightness distributions at *HST* resolution. We attempted to include a large range of luminosity and to exclude problematic objects such as those containing obscuring dust. (The galaxy NGC 4697 shows a dust disk that extends out to 3″4, but the inner 1″0 does not appear to be seriously obscured.)

The stepped gray scales are used in Figure 1 to show the variety of isophote shapes. Some galaxies, like NGC 821, have "disky" isophotes that will produce positive parameters a_4/a, where a_4 is the fourth cosine coefficient in the Fourier expansion of the radial deviations and a is the semimajor axis of the isophote (Lauer 1985; Bender 1988). Others, like NGC 4291, have "boxy" isophotes that will produce negative a_4/a. Boxy isophotes are typically found in galaxies with "core" surface brightness profiles (Faber et al. 1997). A core profile has a break between inner and outer slopes, and the inner logarithmic slope, $\gamma \equiv -d \log I / d \log r$, must be less than 0.3. Similarly, "disky" isophotes are found in "power-law" galaxies, which have no significant break and have steeper slopes. Our sample has six power-law and four core galaxies. We count NGC 4473 as a core because of its surface brightness profile, but it shares many properties with power-law galaxies (see § 5). The core galaxies are grouped on the bottom of Figure 1.

The most luminous core galaxies tend to have a large velocity dispersion and low surface brightness, making measurement of the LOSVDs difficult. Thus, we selected three core galaxies with relatively high surface brightness (NGC 3608, NGC 4291, and NGC 4473). However, we selected one example of a relatively low surface brightness core galaxy, NGC 4649, which has $\mu_V \approx 15.9$ mag arcsec^{-2} at 0″1. It is comparable to M87 in luminosity, and it serves as a test case for measuring absorption-line kinematics in low surface brightness giants.

3. OBSERVATIONS

3.1. *STIS Observations*

Table 2 gives specifications for the spectrograph/grating combinations used. Our STIS observations used only the G750M grating and the STIS CCD detector. The STIS CCD is a 1024×1024 pixel CCD with readout noise around $3.8e^-$ at a gain of 1.0. We binned the CCD by a factor of 2 along the dispersion axis in all of our observations to improve the signal-to-noise ratio (S/N). This raised our reciprocal dispersion to 1.1 Å pixel^{-1}. STIS has a spatial scale of 0″0507 pixel^{-1} in all of the configurations used here.
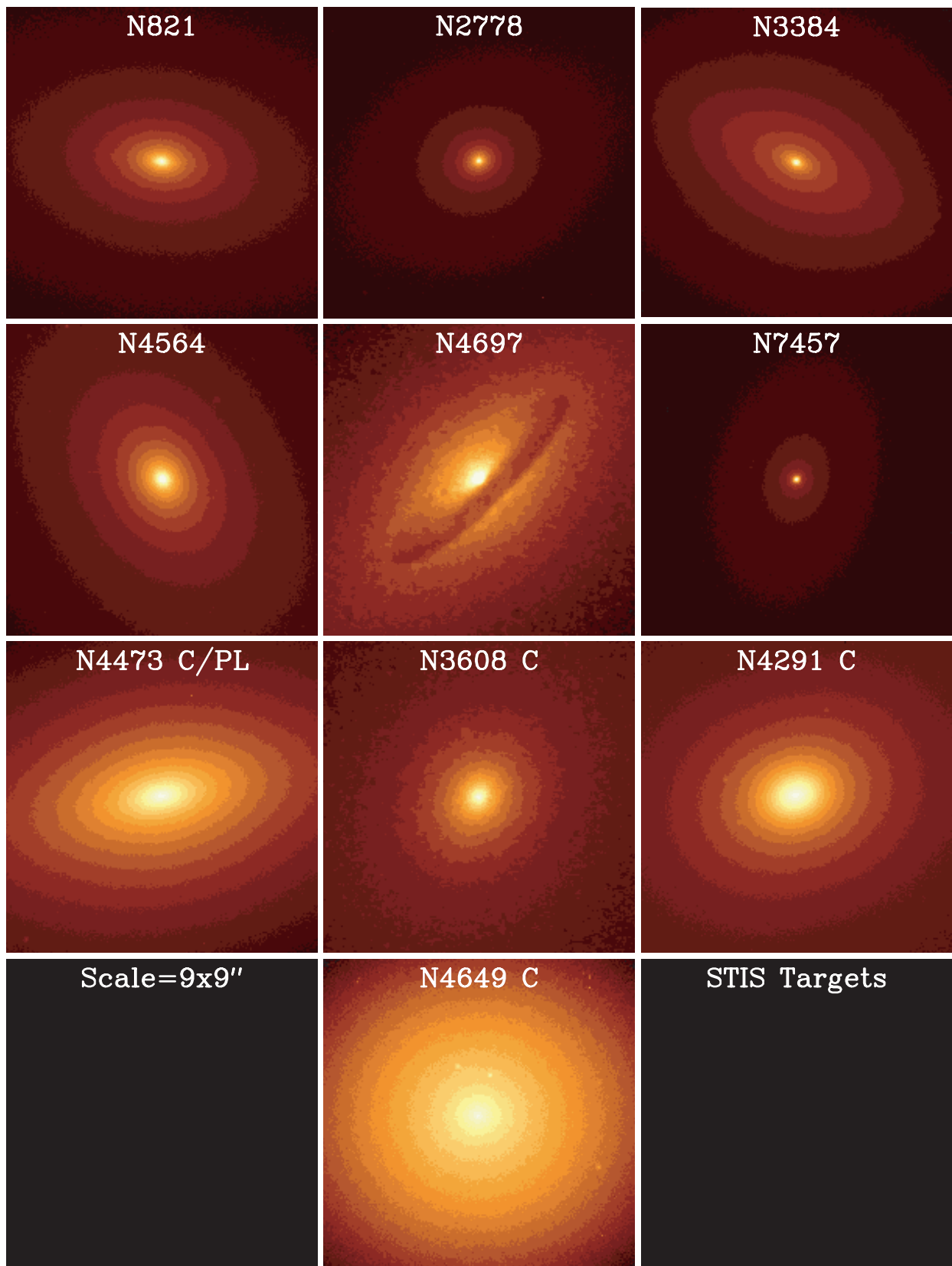
FIG. 1.—*HST* images of our 10 early-type galaxies. These are *V*-band (F555W) WFPC2 images for all except NGC 4564 (F702W) and NGC 4697 (WFPC, deconvolved). Each is a 200×200 pixel subimage, corresponding to $9'' \times 9''$ on the WFPC2 and WFPC images. The label "C" indicates a core-type surface brightness profile (Lauer et al. 1995), while power-law galaxies are labeled only by their NGC number; NGC 4473 is intermediate between core and power law.

PINKNEY ET AL.

TABLE 1
TARGET GALAXIES

Name	Type[a]	M_B[b] (mag)	Profile Type[c]	Distance[d] (Mpc)	Scale[e] (pc arcsec^{-1})	μ_V[f] (mag arcsec^{-2})	P.A.[g] (deg)	r_e[h] (arcsec)
NGC 821	E6?	−20.41	\	24.1	117	14.3	25	50
NGC 2778...............	E	−18.59	\	22.9	111	14.9	40	16
NGC 3384[i]............	SBs0-	−18.99	\	11.6	56	13.7	53	25
NGC 3608...............	E2	−19.86	∩	23.0	111	14.7	75	34
NGC 4291...............	E	−19.63	∩	26.2	127	14.9	110	17
NGC 4473...............	E5	−19.89	\∩	15.7	76	14.7	100	26
NGC 4564...............	E	−18.92	\	15.0	73	14.1	47	20
NGC 4649...............	E2	−21.29	∩	15.9	88	15.9	105	69
NGC 4697...............	E6	−20.24	\	11.7	57	14.4	70	72
NGC 7457...............	SArs0-?	−17.69	\	13.2	64	16.2	130	32

[a] Galaxy type from NED.
[b] Blue absolute magnitude, M_B, calculated using surface brightness fluctuation (SBF) distances.
[c] Surface brightness profile type characterized as either \ (power law) or ∩ (core). Sources are Faber et al. 1997, Byun et al. 1996 (for NGC 4473), and T. R. Lauer 2002, private communication (for NGC 821, NGC 2778, and NGC 4291).
[d] Distances are from SBF measurements in Tonry et al. 2000.
[e] Spatial scale derived from the fifth column.
[f] Central "μ_V" is the V-band surface brightness measured at $r = 0\rlap{.}''1$.
[g] Position angle from RC3.
[h] Effective radius derived from RC3.
[i] NGC 3384 also identified as NGC 3371.

Table 3 gives the details of the *HST* observations. Typically, six orbits were devoted to each galaxy (≈ 2700 s per orbit). However, the galaxies NGC 821, NGC 3384, and NGC 4697 had 11 orbits, and the galaxy NGC 4649 had 18 orbits because of its low surface brightness. Each orbit was divided (CR-split) into two 1350 s exposures except the first orbit of a visit, which had shorter exposures. For the first two visits of the program (NGC 4473 and NGC 821), the galaxy center was only dithered slightly (at the subpixel level) on the chip between orbits. Partway through the program we learned that the CCD had a rapidly varying population of hot and warm pixels. We then requested wider separations between dithers (20 pixels) so that a dark frame could be constructed from the data. Five dither positions were used. The second visit to NGC 821 used wide dithers, so only NGC 4473 did not receive any wide-dither observations.

For one galaxy, NGC 4697, two 1050 s exposures were taken with the G750M in setup 3 (Table 2). Here the spectral range is centered near $\lambda_{\rm cen} = 6581$ Å. We see Hα + [N II] emission lines that allow a useful comparison of gas and stellar kinematics. The reduction and analysis of these data are described elsewhere (J. Pinkney et al. 2003 in preparation).

Table 3 includes a K3 III and a G8 III star observed by us. We use these as LOSVD-fitting templates, for assessing aperture illumination corrections, and for measuring the STIS point-spread function (PSF). We also used HR 7615

TABLE 2
LONG-SLIT SPECTROGRAPH CONFIGURATIONS

Code	Instrument + Grating	Slit Size (arcsec)	$\lambda_{\rm cen}$[a] (Å)	λ Range[a] (Å)	Dispersion^{-1}[b] (Å pixel^{-1})	Comparison Line σ[c] (Å)	Spatial Scale[d] (arcsec pixel^{-1})
1....................	STIS + G750M	52 × 0.1	8561	8275–8847	1.1089	0.45 (17.5)	0.05071
2....................	STIS + G750M	52 × 0.2	8561	8275–8847	1.1089	0.68 (23.8)	0.05071
3....................	STIS + G750M	52 × 0.1	6581	6295–6867	1.1130	0.37 (16.9)	0.05071
4....................	Charlotte + 831g/mm	760 × 0.8	8500	7801–9199	1.44	0.98 (35.)	0.593
5....................	Wilbur + 831g/mm	760 × 0.9	8500	7580–9420	0.909	1.10 (39.)	0.371
6....................	Charlotte + 1200g/mm	760 × 0.9	5175	4689–5661	1.11	0.75 (37)	0.593

NOTE.—Most of the STIS setups used a CCD readout with 2X overbinning along the dispersion and a read noise of $\sim 1e^-$ pixel^{-1}. The Modspec setup values are given by the program "modset" by J. Thorstensen. The slit widths and spectral and spatial resolutions varied for the Modspec observations; characteristic values are shown here.
[a] Central wavelength and wavelength range. STIS values taken from Leitherer et al. 2001, pp. 231 and 234.
[b] Reciprocal dispersion was measured using our own wavelength solutions. The distribution of dispersion solutions for a given data set had $\sigma \approx 0.00015$ Å pixel^{-1}. The average dispersion given in the Handbook for G750M is 1.12 Å pixel^{-1}.
[c] Instrumental line widths measured by fitting Gaussians to emission lines on comparison lamp exposures (values in parentheses are in units of km s^{-1}). This gives an estimate of the instrumental line width for *extended* sources. We use roughly five lines per exposure and at least five measurements per line. In the cases of the G750M setups, the comparison lamp exposures were unbinned, while the galaxy spectra were binned by 2X along the dispersion axis. The 2X binning increases the measured widths by, e.g., $\sim 25\%$ for the $0\rlap{.}''1$ slit and $\sim 3\%$ for the $0\rlap{.}''2$ slit at 8561 Å. Leitherer et al. 2001 (p. 300) give these instrumental line widths for point sources: $\sigma = 13.3$, 15.0, and 16.7 km s^{-1} for the first three G750M setups in this table.
[d] The spatial scale along the slit is constant, but it varies across the slit from one grating to the next. It is $0\rlap{.}''05597$ pixel^{-1} for G750M at 8561 Å and $0\rlap{.}''05465$ pixel^{-1} for G750M at 6581 Å (STIS ISR 98-23).

TABLE 3
STIS Observations

Name	Exposure (s)	Observation Date[a]	P.A.[b] (deg)	ΔP.A.[c] (deg)	Setup Code[d]
NGC 821	27478	1998 Oct 13, 1999 Sep 08	−150	5	1
NGC 2778..............	15026	1999 Jun 03	50	10	1
NGC 3384..............	27744	1998 May 10, 1999 Apr 16	58	5	1
NGC 3608..............	12950	1998 May 14	94	19	2
NGC 4291..............	16013	1998 Apr 21	110	0	2
NGC 4473..............	12840	1997 Dec 04	−100	−20	2
NGC 4564..............	15060	1998 Mar 08	−143	−10	1
NGC 4649..............	46467	1999 Jun 09	95	−10	2
NGC 4697..............	24820	1999 Jul 27, 1999 Aug 20	68	−2	1, 3
NGC 7457..............	15282	1999 Sep 24	130	0	1
HR 7576[e]	5 × 3.2, 5 × 3.2	1999 May 14	−173	...	1, 2
HR 6770	5 × 2.2, 5 × 3.2	1999 Sep 06	54	...	1, 2

[a] The date at the end of the visit.
[b] Position angle of the STIS slit. From the FITS headers.
[c] Difference between the STIS P.A. and the RC3 P.A.
[d] Code for the spectrograph setup used (see Table 2).
[e] Template stars were HR 7576 ($V = 5.03$ mag, K3 III) and HR 6770 ($V = 4.64$ mag, G8 III).

from Bower et al. (2001). The template stars were observed through the same slits that we used for our galaxies. We used two slit apertures in our STIS setups: $52'' \times 0''.1$ and $52'' \times 0''.2$. The aperture point-source throughputs are 64% and 77.8%, respectively, at 8500 Å. The $0''.1$ slit required a PEAKUP, while the $0''.2$ slit did not. We used the $0''.2$ slit for the four core galaxies (NGC 3608, NGC 4291, NGC 4473, and NGC 4649) and the $0''.1$ slit for the six power-law galaxies.

3.2. *Ground-based Observations*

We used the Modular Spectrograph (hereafter Modspec) on the 2.4 m Hiltner Telescope at MDM Observatory for long-slit spectroscopy (Table 4). The camera was equipped with either a thick, front-side–illuminated LORAL 2048^2 CCD (" Wilbur ") or a thinned, back-side–illuminated SITE 1024^2 CCD (" Charlotte "). The LORAL chip had $4.7e^-$ readout noise, while the SITE had $5.45e^-$. The Modspec Ca II setup produces comparable spectral resolution to our STIS + G750M setups (Table 2). Its spatial resolution is worse, of course, varying with seeing in the range $0''.6$–$2''.0$. Our CCDs had pixel scales of $0''.371$ pixel^{-1} (Wilbur) and $0''.59$ pixel^{-1} (Charlotte).

Multiple exposures were taken of each galaxy, with lower surface brightness galaxies receiving more exposures. The slit was placed along the major axis and at least one other position angle (Table 4). Small dithers of the galaxy along the slit were used to remove CCD defects. The galaxy observations were bracketed by star observations to help monitor the seeing and to build a library of template stars for defining the broadening functions in the galaxy spectra. Template exposures were generally less than 1 minute. Calibration frames included Ar comparison lamp spectra, continuum lamp spectra, and twilight sky spectra. Guiding used either starlight that was reflected off of the slit jaws or direct guiding from stars outside of the slit-viewing area. The rms deviations on the sky during the guiding were typically around $0''.3$. We often have a star in the slit along with the galaxy. We can compare the FWHM of the star during a long exposure with the FWHM of a star during a short exposure to check the guiding stability. For a 20 minute exposure, the guiding added about a 10%–20% increase in the FWHM.

4. DATA REDUCTION

4.1. *G750M* Ca II *Spectra*

The STIS data reduction was done with our own FORTRAN programs and FITSIO subroutines (Pence 1998). Our primary reasons for not using CALSTIS (Hodge et al. 1998) within IRAF are (1) a better dark frame can be created out of the data than the weekly darks used by CALSTIS, (2) many features of CALSTIS were not important to us, such as heliocentric correction, and (3) we did not want two-dimensional rectification to be unnecessarily complex.

We began by extracting the raw spectra from the multi-dimensional FITS file. To remove the bias level, we subtracted a constant fit to the overscan region. The overscan was about 1110 DN for galaxy spectra and 1505 DN for flats and comparison lamps, with little variation from one visit to the next.

Subtraction of an accurate dark current was important because the STIS CCD has warm and hot pixels that evolve on timescales of $\lesssim 1$ day. The mean dark current was about 0.007 s^{-1} pixel^{-1}, and this produced about 10 DN pixel^{-1} in our exposures. We used an archival dark only for the two visits that were not dithered (NGC 4473 and NGC 821); for the rest, we created a dark out of the data. This *self-dark* required many iterations. The first dark was a biweight combination (see Beers, Flynn, & Gebhardt 1990) of the individual exposures after masking the pixels within ~25 rows of the galaxy peak. The first dark, although imperfect, was subtracted from each spectrum. We proceeded with the flat-fielding, bad-pixel flagging, and undithering, until a two-dimensional spectrum can be made by combining the exposures. This two-dimensional galaxy spectrum was then deflattened, dithered, and subtracted from the raw spectra. The results contained the dark current, cosmic rays, and some residuals from the first, rough, dark subtraction. These were again biweight combined to form an improved dark. We then repeated reduction with this dark frame to

TABLE 4
Ground-based (MDM 2.4 m + Modspec) Observations

Name	Observation Date[a]	P.A.[b] (deg)	Exposure[c] (s)	Setup Code[d]
NGC 821	1995 Nov	0	6×1600	6
	1995 Nov	85	5×1600	6
NGC 2778..............	1997 Nov	0	23×1200	5
	1997 Nov	70	20×1200	5
NGC 3384..............	1997 Mar	0	8×1200	4
	1997 Jan	10	6×1200	6
	1997 Mar	70	7×1200	4
	1997 Jan	88	6×1200	6
NGC 3608..............	1997 Mar	0	7×1200	4
	1997 Mar	75	9×1200	4
NGC 4291..............	1997 Mar	0	8×1200	4
	1997 Mar	29	2×1200	4
	1997 Apr	70	4×1200	4
NGC 4473..............	1997 Mar	0	12×1200	4
	1997 Mar	22	6×1200	4
	1997 Jan	0	4×1200	6
	1997 Jan	90	7×1200	6
NGC 4564..............	1998 Mar	0	12×1200	5
	1998 Mar	30	8×1200	5
	1998 Mar	70	12×1200	5
NGC 4649..............	1997 Jan	0	9×1200	6
	1997 Mar	22	8×1200	4
	1997 Jan	28	6×1200	6
	1997 Jan	68	9×1200	6
NGC 4697..............	1997 Apr	0	9×1200	4
	1997 Apr	48	9×1200	4
	1997 Apr	70	18×1200	4
NGC 7457..............	1997 Nov	0	20×1200	5
	1997 Nov	70	$6 \times 1200, 6 \times 1500$	4

[a] The year and month of observation.
[b] The position angle of the slit relative to the major axis of the galaxy.
[c] Number of exposures times exposure length.
[d] Code from Table 2 for the spectrograph setup used.

form a second two-dimensional spectrum that was again subtracted from the raws for a third *self-dark* iteration. At least five such iterations were performed to remove residual galaxy signal from the dark. A slice along the spatial axis showed the galaxy profile to dwindle to zero if low-level dark current was correctly subtracted from the final galaxy two-dimensional spectrum. This dark also corrected for any bias pattern on the chip. The final galaxy spectrum was typically more free of deviant pixels than if an archival dark was used.

Within our self-dark iteration loop, the dark subtraction was followed by flat-fielding. The flat-fielding was important because interference fringes become strong for $\lambda > 7500$ Å. Our raw data had about 10% peak-to-peak variations due to fringing (Fig. 2). We used a flat that was a combination of the contemporaneous tungsten flats. These are intended to reduce fringe effects to the 0.9% level (Leitherer et al. 2001). It was difficult to measure fringe residuals in our galaxy spectra, but ratios of flats taken within a visit showed no detectable fringe pattern. In addition, a ratio of flats taken 9 months apart through the $52'' \times 0''.1$ aperture contained a residual fringe pattern at the $\lesssim 1.0\%$ level (Fig. 2). The stability of these tungsten flats is one clue to their effectiveness in our reduction. Another is the shape of the final spectra (Figs. 3 and 4), especially for standard stars, which tend to show a linear continuum with
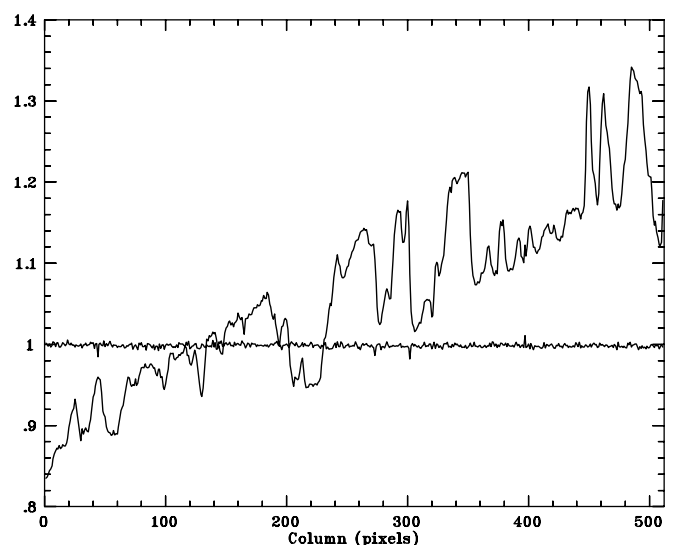

Fig. 2.—Ratio of two CCD flats compared with the original. The wavy line is an average of six rows across the middle of the combined flat for NGC 3384. It was taken with the $52'' \times 0''.1$ aperture and the G750M 8561 Å setup. The relatively flat line is the result of dividing this flat by another taken 9 months later with the same setup.
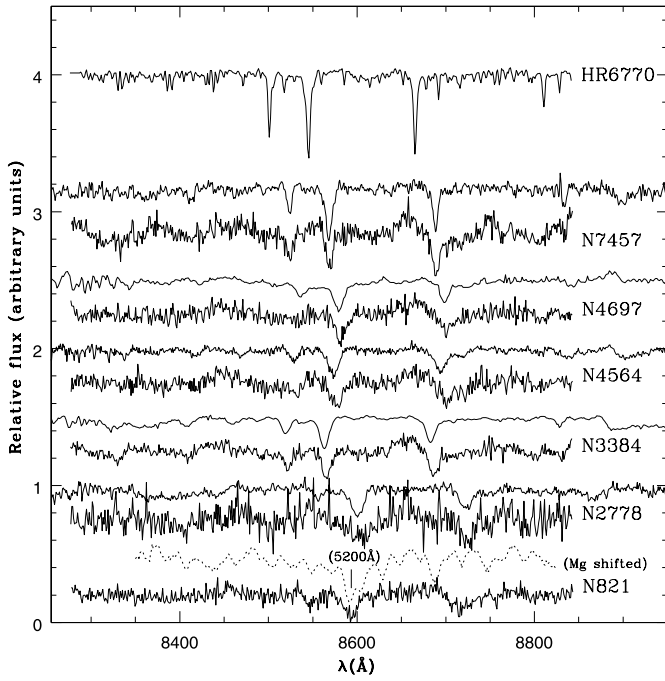
FIG. 3.—Collage of spectra extracted from the central spatial bin for each *power-law* galaxy. For each galaxy, there are a pair of spectra: the top one is from Modspec and the bottom is from STIS. The spectra are the average (biweight) of all exposures. The STIS spectra have been normalized by a linear or parabolic fit to the continuum, while the Modspec spectra were divided by a fit to the local continuum in 100 pixel wide regions, with linear interpolation. The spectra are shifted vertically to avoid overlap. The template star HR 6770 (type G8 III) is shown on top for comparison. For NGC 821, there is no ground-based calcium triplet spectrum, so we have shifted the Mg ($\lambda5175$) spectrum into the plotted wavelength range.
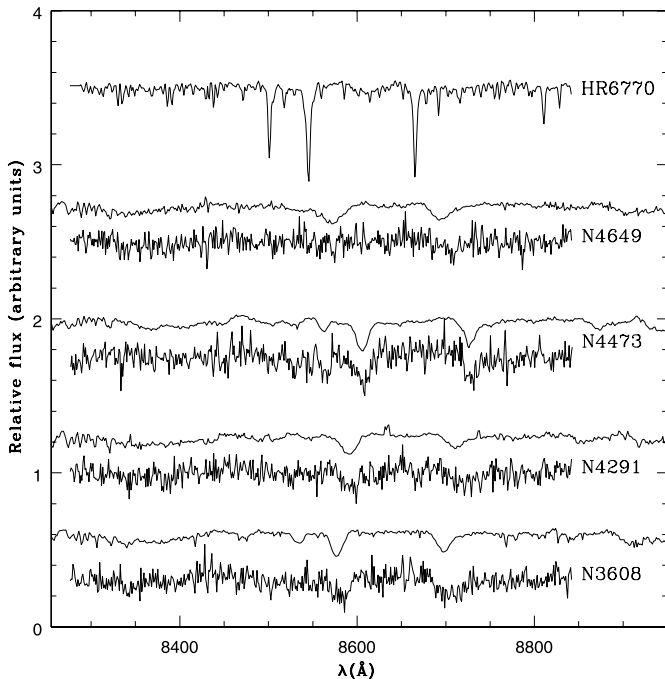
only familiar features superimposed. The overall slope of the galaxy continuum does not have to be perfectly accurate for our purposes, so any color mismatch between the tungsten flat and our galaxies is not problematic.

After flat-fielding, the spectra had to be vertically shifted to a common dither, combined, and rotated. The shifting was done by measuring the peak of the galaxy profile in a 100 column wide region at the center of the CCD. The peak was measured with $\frac{1}{9}$ pixel precision for each frame using a cubic spline interpolation. The spectra were shifted vertically to the same row of pixels, $y = 511.0$. Fractional pixel shifts were allowed in order to provide an accurate superposition, but this created *smearing* (redistribution of counts to neighboring pixels) along columns. The aligned spectra were then combined using the biweight to filter cosmic-ray hits. Since there were five dither positions, every final pixel value was a combination of at least five distinct pixels on the CCD chip. The resulting spectrum has a dispersion with a $0°6$ clockwise tilt relative to the CCD rows. This was removed in the last step using a rotation about the chip center. The rotation adds additional smearing that is spatially periodic; i.e., regions of minimal smearing occur every ~95 pixels. The center of the spectrum, $\lambda = 8559$ Å, was a smearing minimum that happens to fall near the Ca II $\lambda8542$ line for our galaxies.

The final two-dimensional spectra contain imperfections. Figure 5 is an example of a final unsharp-masked, dithered data set for NGC 3384. The box overlay on NGC 3384 shows the $\pm1''$ extent of our one-dimensional extractions from the galaxy center. There is a low-level ($\sigma \approx 1.0$ DN) pattern noise apparent on Figure 5. It is possibly caused by residuals from dark subtraction and/or flat-fielding that are then spatially repeated when the five dithers are combined.

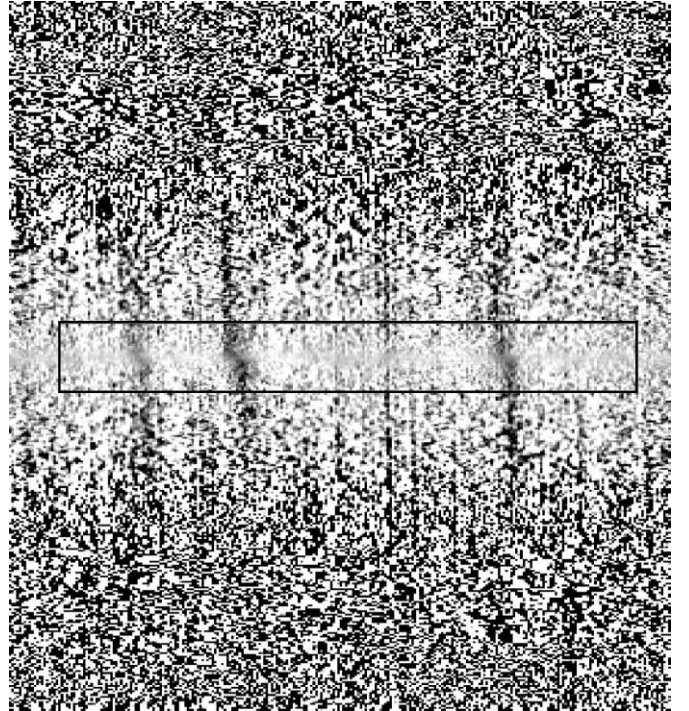FIG. 4.—Same as Fig. 3, except here we show spectra from each *core* galaxy.

FIG. 5.—Unsharp-masked two-dimensional spectrum for NGC 3384. Only a subsection of the CCD is shown. The box is $2''$ tall and shows the vertical extent of the extracted one-dimensional spectra. The Ca II triplet absorption is visible in three vertical bands.

The dark contains charge trails along columns that become more numerous toward the bottom of the chip. These features do not all subtract well, leaving linear features on the spectrogram. Other imperfections are not easily visible. There are typically a dozen bright features between the fiducial bars for an average of 10 exposures of 1350 s each. These are 1–2 pixel events smeared by shifting to cover an area of ~4 pixels. They probably originate in pixels that contain cosmic rays in many of the exposures. (Cosmic-ray hits occur on about 5% of pixels on the raw frames.)

We extracted one-dimensional spectra from the final spectrogram using a biweight combination of rows. Our standardized binning scheme (Table 5) used 1 pixel wide bins near the galaxy center to optimize spatial resolution. All of the bins were contained within $1''.0$ (20 pixels) of the galaxy center. Our dither pattern positioned the galaxy center on the rows $y = 471$, 491, 511, 531, and 551, so that the residuals of the fiducial bars fell as near as $9''.2$ to the galaxy center. These bars did not interfere with our spectroscopy because the S/N generally becomes too poor to measure

kinematics by $r = 1''.5$ for our galaxies. Since our spectral extractions went out 20 pixels from the galaxy center and our maximum dithers were 40 pixels, all of our spectra originate between $y = 450$ and 570 on the chip. This simplified several other aspects of the reduction, including wavelength calibration.

A wavelength solution was obtained for the final galaxy spectra by summing the rows between $y = 450$ and 550 on each of the Pt-Cr/Ne comparison lamp frames. There were typically six unique comparison spectra per visit. The final solution was an average of these six solutions. For each solution, we fitted a line to wavelength versus pixel for 12 lamp lines and got residuals with rms ≈ 0.12 Å. The lines were the 12 brightest after omitting a close double. A typical solution was $y(\text{Å}) = 1.10896 \pm 0.00004x + 8276.26 \pm 0.04$; the errors are the standard deviation from the six solutions. Over the region occupied by the galaxy spectra ($y = 450$–570), the lamp lines exhibit a slight bowing on the CCD that is asymmetric with respect to the central row. We considered errors caused by this bowing. The top dither at $y = 551$ has a zero point that differs by about $+0.17$ Å from that of the central dither ($y = 511$), and the bottom dither at $y = 471$ differs by about -0.11 Å. Thus, by combining vertically shifted dithers, we artificially broaden the lines. The width of the lines increases by less than 0.5% as a result of this co-addition. Since the Ca absorption lines are broader than the lamp lines, their fractional change in width should be even less. The errors in the lamp line centroids caused by the co-addition are small because the shift caused by the top dither will be nearly compensated by the shift from the bottom dither. Any remaining zero-point error from the asymmetry is $\lesssim 0.05$ Å. Finally, the galaxy spectrum was rotated by $\sim 0°.6$, while the comparison spectrum was not. This introduced only negligible errors ($\lesssim 0.01$ Å) in line positions.

4.2. Template Spectra

The template star observations required a different reduction than the galaxies. Five exposures were taken through each of the $52'' \times 0''.2$ and $52'' \times 0''.1$ slits. The exposure times were 2.2 s, so dark subtraction was unnecessary. Between exposures, the star was stepped across the slit by $0''.04$ and $0''.025$ for the $0''.2$ and $0''.1$ slits, respectively. Combining each set of five spectra allowed us to simulate the observation of a diffuse source through both slits. The combined spectrum was then rotated by $0°.6$. Two lamp flats were obtained with exposure times of 142 ($0''.1$ slit) and 84 s ($0''.2$ slit). The flats were also combined and rotated. Next, one-dimensional spectra were extracted from both the star and flat-field spectrograms by averaging the six central rows. The extracted flat was normalized and then divided into the extracted stellar spectrum. The resulting spectra (e.g., HR 6770 in Fig. 3) appear to be corrected of fringing.

The stepping of the stars across the slits allowed us to measure the instrumental broadening of the Ca II triplet absorption lines. The first and last exposures in the $0''.2$ slit had the star positioned at opposite extremes in the slit, a pointing difference of $0''.16$ implying a 1.6 Å centroid shift. However, the measured difference in centroids was only 1.07 Å (38 km s^{-1}) in line centroids. The difference presumably originates in asymmetric vignetting of the stellar PSF by the slit. The Ca lines had widths of about 3.4, 5.5, and 3.9 Å for 8498, 8542, and 8662 Å, respectively, in the individual

TABLE 5
Bins for Spectral Extraction

Name	r_{cen} (arcsec)	Range (pixels)	Width (pixels)
STIS CCD			
cen	0.000	511–511	1
r1	0.051	512–512	1
r2	0.101	513–513	1
r3	0.177	514–515	2
r4	0.304	516–518	3
r5	0.507	519–523	5
r6	0.811	524–530	7
l1	−0.051	510–510	1
l2	−0.101	509–509	1
l3	−0.177	507–508	2
l4	−0.304	504–506	3
l5	−0.507	499–503	5
l6	−0.811	492–498	7
Wilbur			
cen	0.0	300–300	1
r1	0.37	301–301	1
r2	0.73	302–302	1
r3	1.28	303–304	2
r4	2.01	305–306	2
r5	3.10	307–310	4
r6	4.93	311–316	6
r7	7.85	317–325	9
r8	12.23	326–339	14
Charlotte			
cen	0.0	300–300	1
r1	0.59	301–301	1
r2	1.48	302–303	2
r3	2.95	304–306	3
r4	4.72	307–309	3
r5	7.38	310–315	6
r6	11.80	316–324	9
r7	18.29	326–336	11
r8	28.32	337–359	23
r9	44.25	360–390	31
r10	69.03	391–443	52

2.2 s exposures. The combined spectra showed only ∼0.1 Å broadening when summed in the 0″.2 aperture. Thus, there is a $\lesssim 5\%$ broadening of the narrowest stellar Ca line due to the wider of the two slit widths. The broadening of Ca lines in our target galaxies will be even less. Finally, the STIS PSF was also derived from the template star exposures. The method and results are identical to those described by Bower et al. (2001).

4.3. *Ground-based Spectra*

The Modspec data were also reduced with FITSIO routines. The CCD frames were overscan corrected, bias subtracted, and trimmed. The flat frames were constructed out of the twilight sky frames and the continuum lamp frames as follows. We derived a small-scale structure flat from the continuum lamp. The large-scale structure along the dispersion axis was also taken from the continuum lamp. The structure along the spatial axis, however, was taken from the twilight frames. The final flat was the product of these three individual flats.

After flat-fielding, the spectra were rectified. We used wavelength solutions from neon and argon comparison lamps and the traces of several standard-star spectra to define our geometric transformations. Pixel smearing was not as much of a concern with the Modspec data as with STIS because we do not rely on Modspec for high spatial resolution. Therefore, nonlinear transformations were used and spectral images were shifted, aligned, and dispersion corrected as needed before combining into final two-dimensional spectra. Sky spectra were defined on the edges of the chip, where galaxy light was minimal, and subtracted from the two-dimensional spectra.

Table 4 shows our exposure times for each position angle (P.A.) for each galaxy. We took between two and 23 exposures for a given P.A. to reach the desired S/N. As an example, a 1200 s exposure of an elliptical galaxy (NGC 4564 is used here) with an *HST*-measured surface brightness at 1″.0 of $\mu_V = 16.0$ mag arcsec^{-2} will have a Ca spectrum with about S/N ≈ 20.0 Å^{-1} for a spectrum extracted from a 0″.37 wide bin (1 pixel on the Wilbur CCD). For such a galaxy, seven exposures will allow S/N ≈ 50 Å^{-1} to be reached in the central extraction. This is easily sufficient for measuring the h3 and h4 parameters of the LOSVD. The outer parts of the galaxy can be measured with adequate S/N by using broader extraction bins (see Table 6). In the case of NGC 4564, to reach S/N ≈ 25 (giving uncertainties in H3 and H4 of ± 0.05) at a radius where $\mu_V = 19$ mag arcsec^{-2}, a 4 pixel wide bin and seven exposures are sufficient.

4.4. *Imaging*

A luminosity density distribution is needed for the modeling of each galaxy's mass distribution (see Gebhardt et al. 2003a). A nonparametric fit is made to the surface brightness profile, and this is deprojected into luminosity density following Gebhardt et al. (1996). We used primarily WFPC2 images in filters F555W (*V*) and F814W (*I*) from *HST* proposals PID 5512, 6099, 6587, and 6357. For NGC 4697, we used pre-COSTAR WFPC1 data in F555W. The images were typically sums of four or more exposures. Starting with PID 6587, we used subpixel dithers for improved spatial sampling. All WFPC2 images were deconvolved with 40 iterations of Lucy-Richardson deconvolution, while 80 iterations were applied to the WFPC images. Our images are shown out to $r = 4″.5$ in Figure 1 and surface brightness profiles are shown in Gebhardt et al. (2003a). The profiles are actually a composite of *HST* and ground-based data, where the ground-based profile is shifted by a constant to match *HST* at a radius where seeing effects are minimal. The ground-based CCD photometry was taken primarily from Peletier (1989).

For reference, the parameters of the best fit of the photometry to the five-parameter Nuker law (Lauer et al. 1995) are given in Table 6. We show published values from Rest et al. (2001), Ravindranath et al. (2001), and Faber et al. (1997), or, if these are not available, our own fits to the *I*- and *V*-band WFPC2 images. The Nuker law is a double

TABLE 6
NUKER LAW PROFILE FITS

Name	Filter[a]	I_b[b]	r_b[c]	α	β	γ[d]	References
NGC 821	*H*	13.2	1.1	1.0	1.6	0.64	1
NGC 2778.....................	*I*	14.5	0.3	0.3	1.8	0.30	2
NGC 2778.....................	*V*	15.1	0.1	0.4	1.6	0.16	2
NGC 3384.....................	*I*	15.1	2.9	11.2	1.8	0.65	2
NGC 3384.....................	*V*	16.3	2.9	12.0	1.8	0.64	2
NGC 3608.....................	*V*	15.5	0.3	1.1	1.3	0.00	3
NGC 4291.....................	*H*	12.3	0.5	2.1	1.5	0.02	1
NGC 4291.....................	*R*	15.1	0.6	1.4	1.6	0.00	4
NGC 4473.....................	*I*	16.2	5.3	0.7	2.7	0.01	2
NGC 4473.....................	*V*	17.7	6.3	0.7	2.9	0.01	2
NGC 4564.....................	*R*	15.9	1.3	1.4	1.3	0.80	4
NGC 4649.....................	*V*	17.2	3.6	2.0	1.3	0.15	3
NGC 4697.....................	*V*	13.5	2.6	24.9	1.0	0.74	3
NGC 7457.....................	*H*	13.5	0.3	2.3	1.0	0.35	1

NOTE.—These are fits to the surface brightness profile along the major axis.
[a] Filter used: H = F160W(nic), I = F814W, R = F702W, V = F555W.
[b] Surface brightness at the break radius.
[c] Break radius: the radius of the transition between inner and outer power laws.
[d] Inner power-law slope.
REFERENCES.—(1) Ravindranath et al. 2001. (2) T. R. Lauer 2002, private communication. (3) Faber et al. 1997. (4) Rest et al. 2001.

power law given by

$$I(r) = 2^{(\beta-\gamma)/\alpha} I_b \left(\frac{r_b}{r}\right)^\gamma \left[1 + \left(\frac{r}{r_b}\right)^\alpha\right]^{(\gamma-\beta)/\alpha}, \quad (1)$$

where γ is the slope as $r \to 0$, β is the slope at large r, and α determines the sharpness of the break between the two power laws at r_b. These parameters are correlated (see Byun et al. 1996), and the slippery nature of the five-parameter fit allows for occasional sporadic values. These are fits to the major-axis surface brightness distribution. If two sets of parameters are given for a galaxy, we adopt the average for each parameter for the purpose of plotting (§ 6).

4.5. STIS Light Profiles

Our STIS spectra also provide information on the near-infrared surface brightnesses of our galaxies. Figure 6 shows intensity as a function of slit position. The slits were approximately aligned with the major axes (Table 3). We produced intensity profiles in order to check the shifts of our galaxy peaks to a common position, row 511.0. The profiles are slices along the spatial axis of the two-dimensional spectrum, which are each a biweight of at least 10 exposures. The slices are 101 pixels wide (columns 200–300). The peak was defined as the maximum of a smooth, cubic spline fitted to the profile, thus allowing subpixel interpolation. The final two-dimensional spectra were always peaked within 0.4 pixels of row 511.0. For the creation of Figure 6, the fitted peaks were shifted to fall exactly on 511.0 to best demonstrate any asymmetry in the galaxies.

It is worth noting that these STIS data sets are valuable as probes of surface brightness features because total exposure times are over 10 times greater than typical WFPC2 surveys, the near-IR wavelengths are less dust sensitive, and saturation is avoided by dispersing the light. The ordinate of Figure 6 gives the counts obtained in 1350 s ("DN" are equivalent to the number of electrons because gain = 1). However, at least 1010 pixels are averaged to determine each point so that the Poisson errors are actually very small: at 60 DN, the 68% error is only 0.2 DN, or about one-half the size of the plotted points. The kinematics are derived only out to ±20 pixels (1″0).
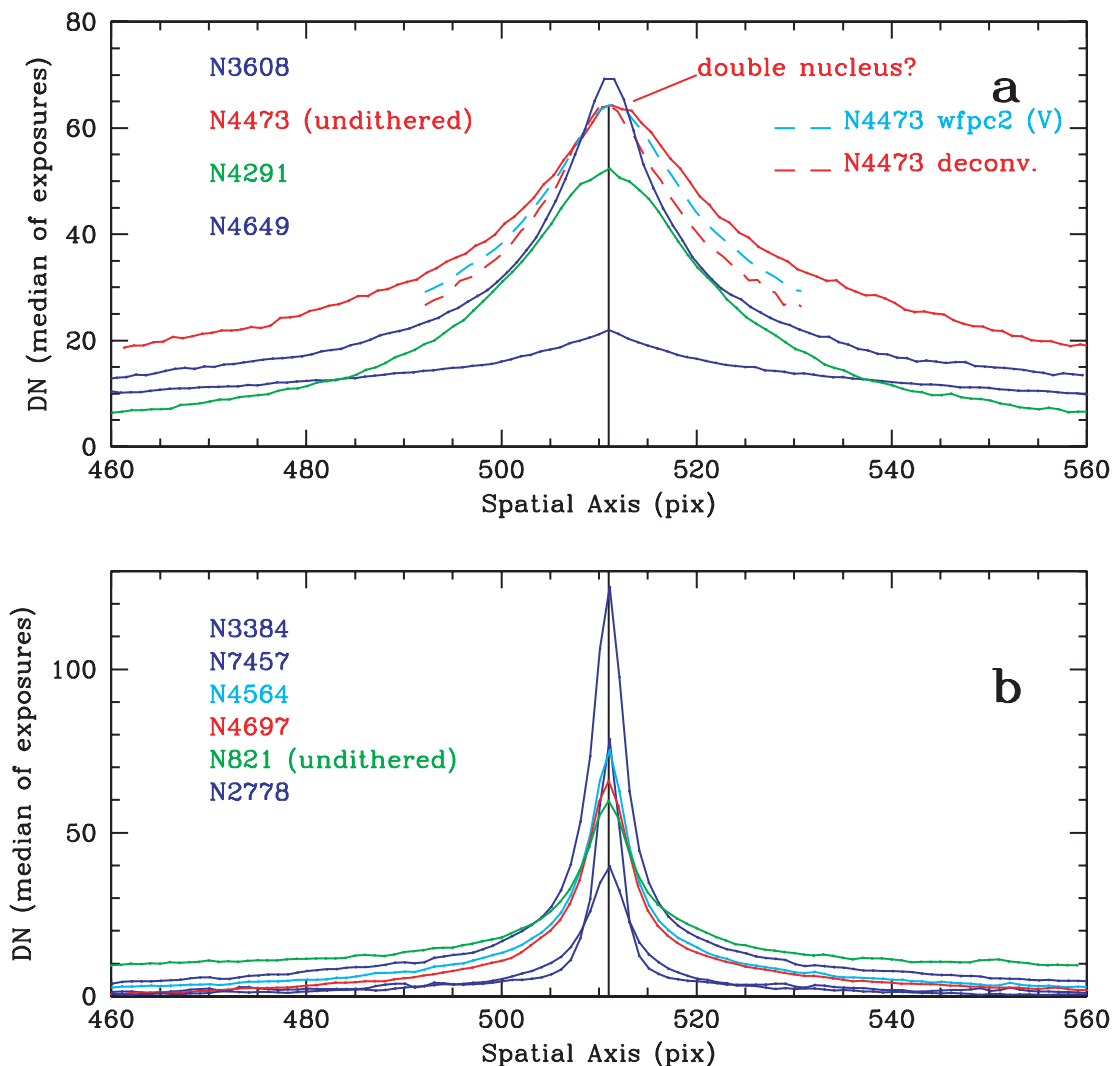

FIG. 6.—Galaxy light profile along the STIS slit (roughly major axis). Columns 200–300 on the STIS chip were averaged, corresponding roughly to the bandwidth 8495–8605 Å. (a) Core galaxies. These were observed with the 52″ × 0″2 STIS slit. The "shoulder" in NGC 4473 is labeled (see § 5.6). In addition, dashed lines are overlayed showing the light in a simulated STIS slit over the WFPC2 data for NGC 4473. (b) Power-law galaxies. These were observed with the 52″ × 0″1 STIS slit.

A point is labeled "double nucleus?" in reference to the note given in Table 1 of Byun et al. (1996). Here we find a significant asymmetry in the two sides of NGC 4473: one side is ∼5 DN higher than the other at $|r| = 2$ pixels. Furthermore, the labeled point deviates from a line connecting the adjacent points by 1 DN, which is also marginally significant. As can be seen in the steep profiles of the power-law galaxies (Fig. 6b), the asymmetric PSF of STIS does not create asymmetries in these light profiles as strong as the one in NGC 4473.

5. KINEMATICS FROM STARS: LOSVD FITTING

The modeling of stellar kinematics requires the derivation of LOSVDs at numerous positions on the galaxy. The STIS spectra are used to sample only $\pm 1''0$ along the major axis, while our Modspec observations sample to 1–2 half-light radii (ranging from $10''$ to $70''$) along the major axis and other position angles. After some experimentation, the binning shown in Table 5 was chosen. It provides the best spatial resolution while maintaining adequate S/N. The first three bins are each 1 STIS pixel wide.

Obtaining internal kinematic information requires a deconvolution of the observed galaxy spectrum using a template spectrum composed of several representative stellar spectra. Both the deconvolution process and the template library are significant issues for obtaining the LOSVD. We deconvolve each spectrum using two different techniques: a maximum penalized likelihood (MPL) estimate that obtains a nonparametric LOSVD and a Fourier correlation quotient (FCQ) technique (Bender 1990). MPL proceeds as follows. We choose an initial velocity profile in bins (the choice of initial profile has no effect on the result). The initial velocity profile convolved with a weighted-average template (discussed below) provides a galaxy spectrum that is used to calculate the residuals to the observed spectrum. The program fits the shape of the LOSVD by subdividing it into 13 velocity bins and varying the counts in these bins while adjusting the template weights to provide the best match to each galaxy spectrum. The exact number of bins has little influence on the final results. Thus, the template mixture can vary from one radius to the next, just as the velocity, velocity dispersion, etc., can. The MPL technique is similar to that used by Saha & Williams (1994) and Merritt (1997). However, our method differs from theirs in that we fit simultaneously for the velocity profile and template weights.

We continuum-divide all template and galaxy spectra. We use a local continuum for the estimate as opposed to a global *n*-parameter fit to the full spectrum. The continuum is estimated by dividing the spectrum up into about 10 wavelength windows, estimating a robust mean (the biweight; see Beers et al. 1990) in each window and interpolating between these values. This mean is measured from the highest $\frac{1}{3}$ of the points to compensate for absorption features. We have tried a variety of continuum estimates (varying the number of local windows and number of points used in the local averaging) and find insignificant differences in the kinematic results.

We use Monte Carlo simulations to measure the uncertainties on the velocity profile bins. For each realization, we generate a simulated galaxy spectrum based on the best-fit velocity profile and an estimate of the rms residual of the initial fit. The initial galaxy spectrum comes from the template star convolved with the measured LOSVD. This provides a galaxy spectrum with essentially zero noise (the noise in the template is insignificant for our purposes). From that initial galaxy spectrum, we then generate 100 realizations and determine the velocity profile, and hence the velocity dispersion, each time. Each realization contains flux values at each wavelength that are chosen from a Gaussian distribution, with the mean given by the initial galaxy spectrum and the standard deviation given by the rms of the initial fit. The 100 realizations of the velocity profiles provide a distribution of values from which we estimate the 68% confidence bands. These velocity profiles and their 68% confidence bands are used directly in the dynamical modeling (Gebhardt et al. 2003).

We wish to compare the MPL-derived LOSVD with those derived using FCQ (see above). To do this, we must convert the nonparametric LOSVDs into GH polynomials. We use the least-squares estimator MRQMIN from Press et al. (1992) to find the best fit to this parameterization:

$$f(y) = I_0 \exp\left(-\frac{y^2}{2}\right)[1 + h_3 H_3(y) + h_4 H_4(y)], \quad (2)$$

where the mean velocity v_{fit} and velocity dispersion σ_{fit} are contained within $y = (v - v_{\text{fit}})/\sigma_{\text{fit}}$. I_0 is the amplitude of the LOSVD at $y = 0$. The coefficient h_3 multiplies the asymmetric deviations from a Gaussian (i.e., skewness), while H4(y) parameterizes symmetric deviations from a Gaussian (kurtosis). The definitions of H_3 and H_4 are given in BSG94. The first and second moments of the LOSVD will differ from v_{fit} and σ_{fit} when h_3 and h_4 are nonzero. For example, the σ_{fit} is ∼10% smaller than the second moment about the mean when $h_4 = 0.1$ and ∼5% smaller for $h_3 = 0.1$. Similarly, v_{fit} will be ∼15% larger than the first moment for $h_3 = -0.1$ (BSG94).

We tabulate the first four terms of the GH expansion of the LOSVD for each galaxy in Tables 7 and 8. We use v_{fit} and σ_{fit} rather than corrected values (e.g., $v_{0,c}$ and $\sigma_{0,c}$ used in Joseph et al. 2001) for reasons listed in BSG94 and for the most direct comparison to published results. Hereafter we refer to v_{fit} and σ_{fit} as v and σ. We found that FCQ and MPL gave consistent profiles and errors. Figure 7 plots the first four GH moments for both FCQ and MPL for NGC 4473. FCQ showed more scatter than MPL in galaxies with poorly defined lines (e.g., NGC 4649). We plot only the MPL-derived v, σ, h3, and h4 against r in §§ 5.1–5.10.

The Monte Carlo simulations used to measure the uncertainties also provide an estimate of the estimator biases. This bias may be important for the dynamical models since the shape of the velocity profile at some level determines the internal orbital structure. Furthermore, Joseph et al. (2001) argue that H_4 estimated from FCQ is biased to lower values when the galaxy dispersion is low (less than 100 km s^{-1}). The Monte Carlo simulations provide the most accurate estimate of any biases since they simulate the exact instrumental setup and spectral sampling. We find little to no bias in our MPL estimates of the first four GH moments. Another way to check biases and confidence bands is to fit to simulated data sets. We have done this for both FCQ and MPL. The FCQ results are similar to what is discussed in Joseph et al. (2001); that is, for galaxies with dispersion below 100 km s^{-1}, H_4 is biased to lower values by about 0.04 for S/N = 30 Å^{-1}, which is typical for these data. Figure 8 shows the results for MPL run-on simulations using the same setup we used on the STIS galaxies and for S/N = 15,

TABLE 7
GROUND-BASED (MDM 2.4 m + MODSPEC) KINEMATICS

Name	P.A._rel[a]	Sym?[b]	r^c (arcsec)	v^d (km s^{-1})	ϵ_v	σ^e (km s^{-1})	ϵ_σ	h3[f]	ϵ_{h3}	h4[g]	ϵ_{h4}
NGC 821 (Mg).............	0	Yes	0.0	−7.	4.	235.	3.	0.02	0.02	−0.07	0.02
	0	Yes	0.6	25.	7.	231.	6.	−0.02	0.03	−0.01	0.03
	0	Yes	1.2	51.	6.	215.	6.	−0.07	0.02	0.02	0.03
	0	Yes	1.8	58.	5.	203.	7.	−0.07	0.03	0.05	0.03
	0	Yes	2.7	59.	5.	204.	5.	−0.04	0.03	0.04	0.03
	0	Yes	4.4	62.	5.	198.	6.	−0.04	0.03	0.04	0.03
	0	Yes	7.1	71.	5.	187.	7.	−0.04	0.03	0.05	0.03
	0	Yes	11.2	64.	6.	195.	7.	0.01	0.03	0.03	0.03
	0	Yes	18.0	75.	6.	179.	9.	−0.02	0.04	0.08	0.04
	0	Yes	28.3	73.	9.	157.	11.	−0.10	0.04	0.00	0.04

NOTE.—Table 9 is published in its entirety in the electronic edition of the *Astrophysical Journal*. A portion is shown here for guidance regarding its form and content.
[a] Position angle of slit relative to the major axis.
[b] "Yes" indicates that the spectra from the two sides of the galaxy center have been symmetrized.
[c] Radius.
[d] Line-of-sight velocity from fit to eq. (1) (see text).
[e] Velocity dispersion from fit to eq. (1) (see text).
[f] Third GH coefficient.
[g] Fourth GH coefficient.

30, and 60 Å^{-1}. The MPL results show no bias in either H_3 or H_4. In addition, the uncertainties determined from the simulated data sets agree with those determined from the galaxy spectra at the same S/N; i.e., at S/N = 40 Å^{-1}, we obtain MPL uncertainties on H_3 and H_4 to around 0.02. After correcting for the bias in FCQ, the uncertainties on H_3 and H_4 are similar.

While we report the first four GH moments in Table 8, we use the nonparametric velocity profile for the dynamics. These moments are reported only to provide a simple parameterization of the velocity profile for comparison and correlation studies. An important difference is that the non-parametric velocity profiles are not allowed to be negative at any point. Using only the first four moments of a GH expansion will allow negative portions of the velocity profile. This is unphysical, but the effect should be small (at least when h_3 and h_4 are small). Thus, the optimal comparison for the dynamical models is to use nonnegative velocity profiles.

We now discuss each individual galaxy. We will include special points of interest, as well as a comparison to published kinematics, where available.

5.1. NGC 821

NGC 821 is classified as E6? (de Vaucouleurs et al. 1991, hereafter RC3). The uncertainty is likely to originate from its resemblance to an S0. NGC 821 is a clear example of an elliptical galaxy with disky isophotes (Lauer 1985; Bender, Döbereiner, & Möllenhoff 1988; Nieto et al. 1991). As is

TABLE 8
STIS-MEASURED KINEMATICS FROM Ca II

Name	P.A.[a]	Sym?[b]	r^c (arcsec)	v^d (km s^{-1})	ϵ_v	σ^e (km s^{-1})	ϵ_σ	h3[f]	ϵ_{h3}	h4[g]	ϵ_{h4}
NGC 821	−150.	No	0.00	−1.	19.	248.	16.	0.02	0.05	−0.04	0.05
	−150.	No	0.05	−65.	19.	273.	21.	0.06	0.05	−0.07	0.05
	−150.	No	0.10	−101.	20.	244.	20.	0.05	0.05	−0.02	0.07
	−150.	No	0.17	−81.	15.	186.	12.	0.04	0.03	0.00	0.05
	−150.	No	0.30	−47.	24.	177.	21.	0.10	0.07	0.02	0.08
	−150.	No	0.50	−47.	32.	206.	19.	0.05	0.07	−0.08	0.08
	−150.	No	0.82	−143.	51.	233.	47.	0.09	0.15	0.04	0.16
	−150.	No	−0.05	5.	20.	229.	16.	−0.08	0.05	−0.05	0.05
	−150.	No	−0.10	62.	20.	218.	18.	−0.11	0.06	−0.08	0.05
	−150.	No	−0.17	68.	25.	235.	20.	−0.14	0.06	−0.10	0.05

NOTE.—Table 10 is published in its entirety in the electronic edition of the *Astrophysical Journal*. A portion is shown here for guidance regarding its form and content.
[a] Position angle of STIS slit.
[b] "Yes" indicates that the spectra on the two sides of the galaxy center have been symmetrized.
[c] Radius.
[d] Line-of-sight velocity from fit to eq. (1).
[e] Velocity dispersion from fit to eq. (1).
[f] Third GH coefficient.
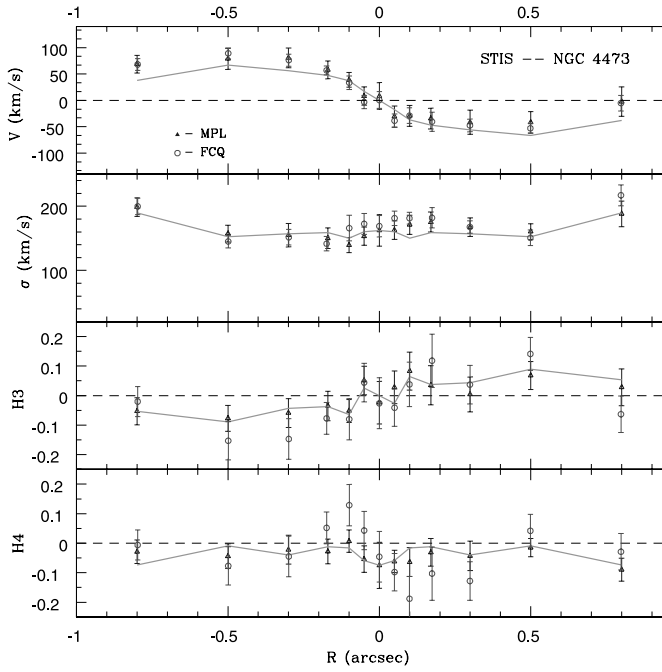[g] Fourth GH coefficient.

Fig. 7.—Comparison of FCQ (*circles*) and MPL (*triangles*): kinematic profiles for NGC 4473. These parameters were derived from unsymmetrized spectra from STIS. From top to bottom, we show mean velocity, velocity dispersion, h3 (3rd coefficient from the GH expansion), and h4 (4th coefficient). The solid lines are derived from the symmetrized LOSVD from MPL. [*See the electronic edition of the Journal for a color version of this figure.*]

typical of such galaxies, it has a power-law surface brightness profile at *HST* resolution (Ravindranath et al. 2001).

NGC 821 is not detected in X-rays (Pellegrini 1999) or in Hα (Macchetto et al. 1996). It also does not appear to contain dust (Forbes 1991) although it is detected by *IRAS* in 100 μm (Roberts et al. 1991). Trager et al. (2000) estimate the average age of its stellar population to be 8 Gyr.

Kinematics shows NGC 821 to be a fairly rapid rotator; Nieto, Capaccioli, & Held (1988) and Nieto, Poulain, & Davoust (1994) measure $(v_{max}/\sigma)^* \simeq 0.71$, and we find 0.75 using our higher STIS v_{max} (Table 10) and $\simeq 0.54$ for our ground-based data (Table 9). We get $v_{max}/\sigma \simeq 0.4$ (Tables 10 and 9), which is lower than previous values (0.49 in Bender 1988; 0.65 in Busarello, Longo, & Feoli 1992).

Our kinematic profiles from Modspec (Fig. 9) are similar to those of BSG94. Both show that the rotation rises quickly to $\sim$60 km s^{-1} at 2$''$. The STIS kinematics shows the largest velocity gradient at 0$\overset{''}{.}$17 in the sample (Table 10). Furthermore, h3 nicely mirrors the velocity profile, as is typical in a rotating, edge-on elliptical. Our ground-based h4 shows a different behavior than in BSG94: we find positive values at $r > 2''$ and negative values in the central bin, whereas BSG94 finds only h4 $\lesssim 0$. Our values are probably more reliable in this case because we have a longer effective exposure time. The main difference between our data and others is the central rise in velocity dispersion. We measure a higher ground-based value, 235 ± 2 km s^{-1}. McElroy's (1995) weighted average of published velocity dispersions was 207 km s^{-1}, and Hypercat (Prugniel et al. 1998) gives the average of 12 velocity dispersions to be 209 km s^{-1}. Our Modspec value does not exceed our central STIS measurement (248 ± 16 km s^{-1}) and may simply be a result of good seeing. When we measure the rms dispersion within a slit aperture of length $2r_e$ (i.e., σ_e), we find 209 km s^{-1}, in agreement with the published averages.

5.2. *NGC 2778*

NGC 2778 is the second least luminous elliptical galaxy in the sample with $M_B = -18.6$ mag. It is located close to NGC 2779 in a group. Trager et al. (2000) estimate the ages of its stars to be only 6.0 Gyr. Its isophotes indicate an E2

TABLE 9
SUMMARY OF MODSPEC KINEMATICS

Name	$\sigma_{0,GB}$[a] (km s^{-1})	$\bar{\sigma}$[b] (km s^{-1})	σ_e[c] (km s^{-1})	$v_{max,GB}$[d] (km s^{-1})	$v_{max}/\bar{\sigma}$[e]	$(v_{max}/\bar{\sigma})^*$[f]	ϵ[g]	$h4_{0,GB}$[h]	$\langle h3 \rangle$[i]
NGC 821	235 (3)	192 (21)	209	74 (6)	0.39 (0.05)	0.54	0.34	−0.07 (0.02)	−0.03 (0.04)
NGC 2778..............	202 (10)	179 (52)	175	85 (14)	0.47 (0.16)	0.85	0.24	−0.06 (0.04)	−0.04 (0.07)
NGC 3384..............	134 (2)	119 (7)	143	107 (8)	0.90 (0.09)	0.99	0.45	−0.05 (0.01)	−0.04 (0.10)
NGC 3608..............	181 (5)	150 (12)	182	24 (5)	0.16 (0.04)	0.31	0.21	−0.08 (0.02)	−0.01 (0.03)
NGC 4291..............	262 (12)	183 (18)	242	79 (10)	0.43 (0.07)	0.71	0.27	−0.04 (0.03)	−0.05 (0.02)
NGC 4473..............	183 (7)	197 (10)	190	75 (4)	0.38 (0.03)	0.47	0.40	−0.00 (0.02)	−0.11 (0.02)
NGC 4564..............	171 (6)	112 (17)	162	147 (4)	1.31 (0.20)	1.18	0.55	−0.01 (0.02)	−0.02 (0.04)
NGC 4649..............	373 (9)	318 (37)	375	93 (27)	0.29 (0.09)	0.65	0.16	0.00 (0.02)	−0.04 (0.02)
NGC 4697..............	157 (5)	145 (5)	177	101 (13)	0.70 (0.09)	0.84	0.41	−0.04 (0.03)	−0.15 (0.03)
NGC 7457..............	73 (3)	63 (3)	67	40 (7)	0.63 (0.12)	0.69	0.46	0.01 (0.03)	−0.02 (0.04)

[a] Dispersion measured in central Modspec bin with error from LOSVD fitting.

[b] Dispersion averaged along the Modspec slit, major axis, for $r > 2\overset{''}{.}0$, using symmetrized LOSVDs and an $\approx 1\overset{''}{.}0$ slit width. The error is the standard deviation of averaged values. Only three numbers are averaged for NGC 2778 (the six measurements outside of $r = 2\overset{''}{.}0$ are symmetrized). The other galaxies include four to eight numbers in the average.

[c] Effective dispersion: the rms velocity relative to the systemic velocity of the galaxy, averaged over a slit width of $\sim 1''$ extending to R_e.

[d] Maximum rotational velocity from symmetrized Modspec data. Implausible maxima were discarded in the case of NGC 821, NGC 4649, and NGC 4697.

[e] Ratio of maximum rotation to $\bar{\sigma}$. The v_{max} comes from the ground-based data.

[f] The ratio of $v_{max}/\bar{\sigma}$ to the $v/\bar{\sigma}$ expected for an oblate, isotropic rotator calculated as $\sqrt{\epsilon/(1-\epsilon)}$, where ϵ is the isophote ellipticity.

[g] Ellipticity $(1 - b/a)$ from Bender 1988, Faber et al. 1997 (NGC 7457), Lauer et al. 1995 (NGC 3608), and Peletier et al. 1990 (NGC 2778). We measured ϵ for NGC 4291 and NGC 3384 using WFPC2 F555W images.

[h] Fourth GH coefficient from the $r = 0\overset{''}{.}0$ bin of the major-axis spectrum.

[i] Third GH coefficient averaged over $r > 2\overset{''}{.}0$ using the symmetrized, major-axis LOSVD. The error is the standard deviation of the mean.
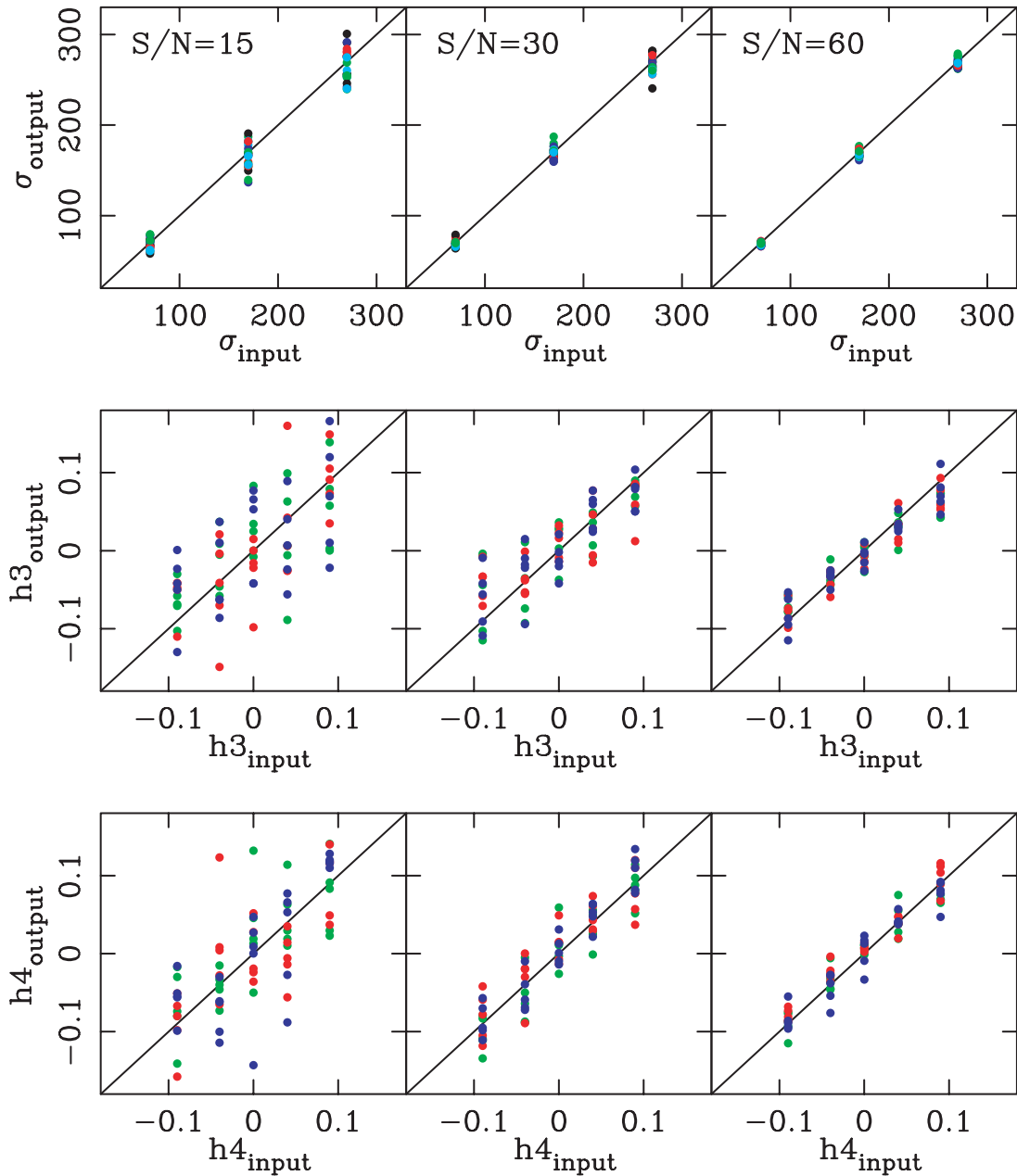
Fig. 8.—Investigation of bias in MPL estimates of GH parameters. From top to bottom, we show velocity dispersion, h_3 (3rd coefficient from the GH expansion), and h_4 (4th coefficient). Each point is a different realization of a broadened template spectrum with noise added. The S/N of the input spectra increases to the right in each row of panels. In the top three panels, the colors light blue, blue, black, red, and green represent h_4 of -0.09, -0.04, 0.0, 0.04, and 0.09, respectively. In the bottom six panels, green stands for $\sigma_{input} = 70$ km s^{-1}, red for 170 km s^{-1}, and blue for 270 km s^{-1}.

morphology with a power-law profile (Peletier et al. 1990; T. R. Lauer 2002, private communication).

Our STIS observations for this galaxy were the only ones taken in Backup Guiding Mode during the *HST* visit. During galaxy acquisition, only one of the two guide stars was found so that drifting about the roll axis was only constrained by gyros. Our parallel observations with the WFPC2 show virtually no change in the centroid of a galaxy image between the first and last (6th) orbit. Since the PC chip is about as far from the guide star as the STIS slit, there was probably no significant error in the STIS guiding.

Davies et al. (1983), González (1993), and Fisher, Illingworth, & Franx (1995) all provide kinematic profiles

for NGC 2778. These rotation curves extend beyond ours to $\sim 25\rlap{.}{''}0$. The maximum rotation velocity, ~ 100 km s^{-1}, is reached by about 5$''$. No rotation was observed along the minor axis; the galaxy is approximately an oblate, rapid rotator (Jedrzejewski & Schechter 1989). All dispersion profiles show a steep rise from $\sigma \approx 100$ to 200 km s^{-1} in the inner 5$''$ (see Fig. 10). This galaxy has the greatest deviation from the M_{BH}-σ relation in our sample: it has a small BH mass for its effective dispersion. The low surface brightness (see Fig. 6) and poorly resolved sphere of influence ($GM_{BH}/\sigma^2 \approx 0\rlap{.}{''}02$) make the BH detection in NGC 2778 relatively uncertain (Gebhardt et al. 2003).

TABLE 10
SUMMARY OF STIS KINEMATICS

Name	$\sigma_{0,STIS}$[a] (km s^{-1})	v_{max}[b] (km s^{-1})	$v_{max}/\sigma_{0,STIS}$[c]	v_{grad}[d] (km s^{-1} arcsec^{-1})	$h4_0$[e]	$h4_3$[f]
NGC 821	248 (16)	103 (23)	0.42 (0.10)	510	−0.04 (0.05)	−0.05 (0.03)
NGC 2778...............	200 (29)	61 (18)	0.43 (0.09)	129	−0.15 (0.17)	−0.08 (0.08)
NGC 3384...............	128 (8)	85 (10)	0.83 (0.08)	414	−0.04 (0.07)	−0.06 (0.03)
NGC 3608...............	296 (27)	28 (20)	0.09 (0.07)	113	−0.13 (0.08)	−0.08 (0.04)
NGC 4291...............	306 (35)	74 (18)	0.26 (0.04)	410	−0.00 (0.07)	−0.04 (0.05)
NGC 4473...............	162 (25)	67 (13)	0.46 (0.08)	278	−0.06 (0.04)	−0.06 (0.03)
NGC 4564...............	220 (20)	90 (34)	0.67 (0.06)	218	0.00 (0.03)	−0.01 (0.03)
NGC 4649...............	547 (101)	145 (70)	0.27 (0.14)	403	−0.07 (0.08)	−0.07 (0.04)
NGC 4697...............	171 (10)	110 (21)	0.64 (0.13)	374	0.14 (0.06)	0.10 (0.03)
NGC 7457...............	105 (8)	8 (7)	0.38 (0.07)	11	0.01 (0.05)	−0.03 (0.03)

[a] Dispersion measured in the central STIS bin with error from LOSVD fitting.

[b] Maximum rotational velocity from symmetrized STIS data. Points with large scatter were ignored in the case of NGC 821 and NGC 2778.

[c] Ratio of maximum rotation (over all data) and central STIS dispersion.

[d] Velocity "gradient" is measured as the maximum of v17/0.17 or v30/0.3, where v17 is the symmetrized rotation velocity at 0″.17 and v30 is the rotation at 0″.30. The entire rotation curve is used to define the galaxy's systemic velocity, not the central bin.

[e] The value of h4 in the central STIS bin ($r = 0″.0$).

[f] The weighted mean of the three central h4 values ($r = 0″.0$, $r = \pm 0″.05$, not symmetrized).

5.3. *NGC 3384*

NGC 3384 is classified as SB(s) (RC3). It is in the Leo I Group, neighbored closely by the elliptical M105 (NGC 3379) and the spirals M95 and M96. It appears to have been named redundantly in the NGC as NGC 3371. Several H I clouds orbit around NGC 3384 and NGC 3379 in a 200 kpc diameter ring formation (Schneider 1985). The H I has been interpreted as gas stripped during an encounter between NGC 3384 and the spiral NGC 3368 (Rood & Williams 1985). The inner regions of NGC 3384 appear largely free of interstellar matter (ISM): Tomita et al. (2000) find no dust in WFPC2 color excess images.

In the WFPC2 *V* and *I* images (Fig. 1), NGC 3384 appears consistent with a lenticular morphology. The Nuker law profile shows a rapid transition ($\alpha = 11.2$) between the inner cusp region ($\gamma = 0.6$) and the outer power
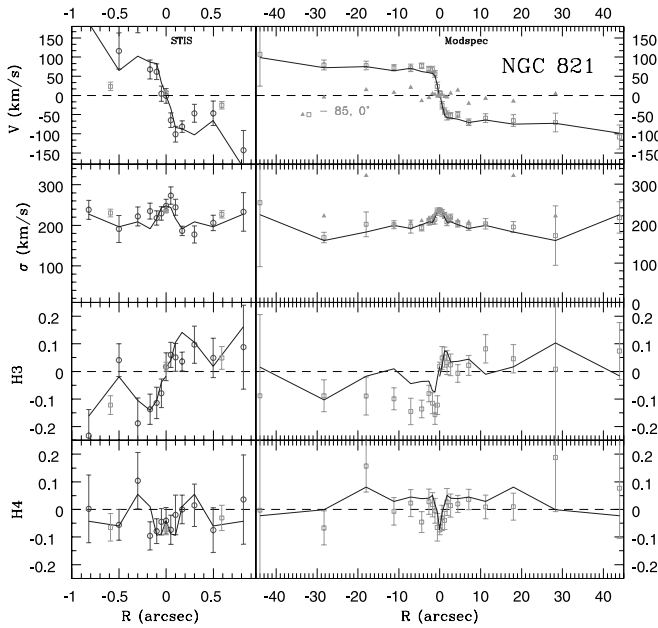

FIG. 9.—Kinematic profiles for NGC 821. From top to bottom, we show mean velocity, velocity dispersion, h3 (3rd coefficient from the GH expansion), and h4 (4th coefficient). *Left:* Major-axis data from $r < 1″.0$. The solid lines are derived from the symmetrized LOSVD from STIS Ca II data. The circles are unsymmetrized data from STIS Ca II. The squares are ground-based, unsymmetrized data. *Right:* Entire radial extent of only the ground-based Modspec data. Again, a solid line connects the symmetrized, major-axis data, and the squares represent unsymmetrized, major-axis (P.A. = 0°) data. Other symbols are labeled by the rotation of the slit with respect to the galaxy's major axis, in degrees. For plotting purposes, the prograde side is always on the right ($r > 0$). For NGC 821, both ground-based position angles are from spectra centered on Mg *b*. [*See the electronic edition of the Journal for a color version of this figure.*]
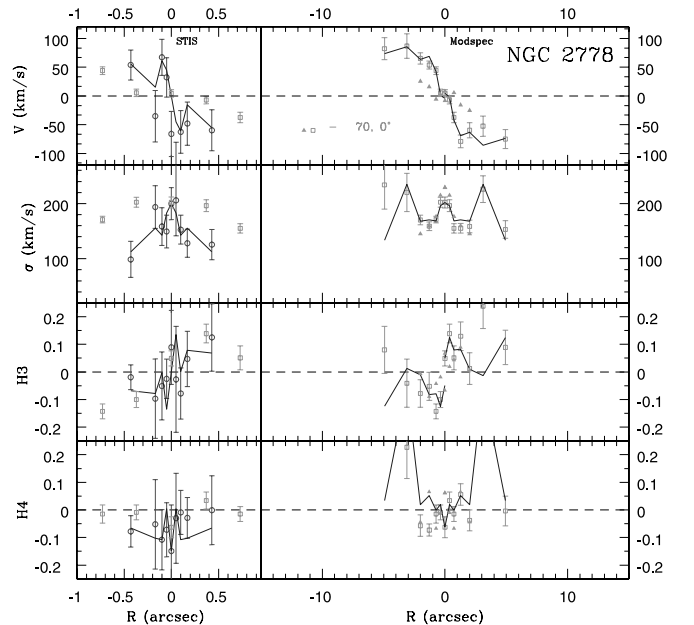

FIG. 10.—Kinematic profiles for NGC 2778 (see Fig. 9 for the meaning of the symbols). For NGC 2778, all ground-based position angles are from Ca spectra. [*See the electronic edition of the Journal for a color version of this figure.*]
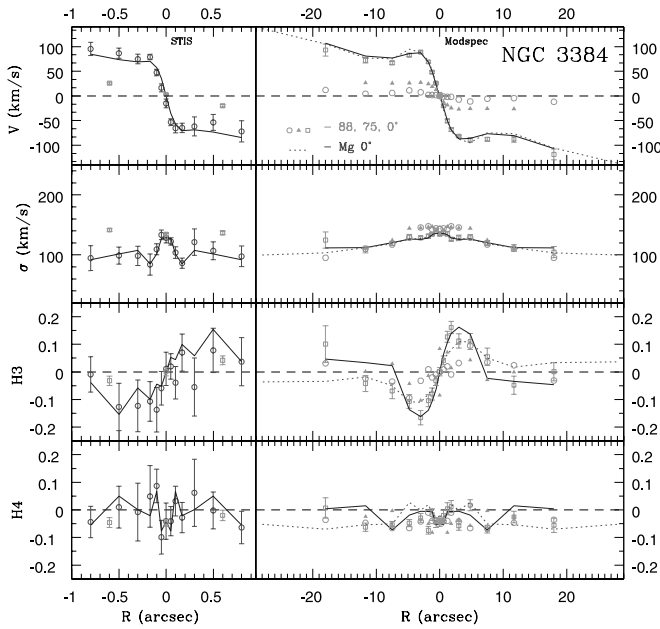
FIG. 11.—Kinematic profiles for NGC 3384 (see Fig. 9 for the meaning of the symbols). For NGC 3384, the dashed line (P.A. = 0°) and P.A. = 88° circles are Mg spectra. All others are Ca spectra. [*See the electronic edition of the Journal for a color version of this figure.*]

law ($\beta = 1.8$) at the break radius $r_b = 2\rlap{.}''9$ (T. R. Lauer 2002, private communication). There also appears to be light in excess of the Nuker law at $r \lesssim 0\rlap{.}''3$. Tomita et al. (2000) use the V and I images to search for dust and blue nuclei. They suspect a blue nucleus in NGC 3384 but claim that it is uncertain because the center is saturated on the PC. High-resolution, ground-based imaging also hints at a nucleus (Kormendy 1985). Our deconvolved surface brightness profiles show a nearly flat $V-I$ profile. Our near-infrared light profile along the STIS slit (which is *not* saturated) shows a strong central peak, but not necessarily a stellar nucleus (Fig. 6). In addition, we do not see Paschen absorption in our Ca II spectra, which would indicate a young stellar population.

NGC 3384 has the highest S/N ($\gtrsim 40$ in central bins) among our STIS data sets as a result of its high surface brightness ($\mu_{V,0.1} = 13.7$ mag arcsec^{-2}) and 11 orbits of exposure (Table 3). Our ground-based kinematics is also of high quality (Fig. 11). We have both Ca II triplet (*solid line*) and Mg b (*dashed line*) data along the major axis. The results we obtain from these two wavelength ranges are consistent.

Our Modspec kinematics for NGC 3384 can be compared to the integral field spectroscopy of de Zeeuw et al. (2002) and to long-slit spectroscopy by Fisher (1997) and Busarello et al. (1996). All rotation velocity curves peak at $r \sim 3\rlap{.}''0$, followed by a decrease. Then, beyond $10''$, the rotation climbs again. Such an "overshoot" is seen in other S0 galaxies, most notably NGC 4111, and about five to 10 of the 18 S0 galaxies studied by Fisher (1997) display some sort of overshoot or kink in their rotation at $\sim 5''$. De Zeeuw et al. (2002) and Fisher (1997) plot minor-axis profiles that indicate that the rapidly rotating disk component has a lower velocity dispersion than the bulge. This is also seen in our $75°$ and $88°$ rotation curves, which show a higher dispersion beyond $2''$ than the major-axis data (Fig. 11). Thus, it appears that a cold stellar disk contributes differentially to

the total light, increasing the fitted rotation velocity and decreasing the dispersion at small radii. At STIS resolution, however, the major-axis dispersion profile shows a distinct peak at $r < 0\rlap{.}''2$. The stellar disk also contributes to the strongly asymmetric LOSVDs: our data show a peak h3 value of 0.15 along the major axis, the highest h3 in our sample after NGC 4697. Our ground-based h4 values are systematically lower than those of de Zeeuw et al. (2002) and Fisher (1997), but all show a dip at $r < 2''$.

NGC 3384 has some of the observed characteristics of a *pseudobulge*, i.e., a high-density central mass component that resembles a bulge but that is thought to have been built by the inward transport of disk gas by (in the present case) a bar. This secular process is qualitatively different from the classical picture in which bulges form on approximately a collapse timescale by violent relaxation and dissipation in a galaxy merger. Pseudobulge characteristics of the present galaxies are discussed in Kormendy et al. (2003), and more general reviews of pseudobulges are given in Kormendy (1993) and Kormendy & Gebhardt (2001). In essence, pseudobulges are left with some memory of their origin: they have disky structural properties. In NGC 3384, the pseudobulge dominates the light at radius $r < 6''$, i.e., interior to the bar, which is most important at $r \sim 10''$–$20''$ (Busarello et al. 1996; Jungwiert, Combes, & Axon 1997). In NGC 3384, the evidence for a pseudobulge includes the highest v/σ value in Table 10, an unusually high $(v/\sigma)^*$ value in Table 9, and the observation that the "bulge" is almost as flattened as the disk (its ellipticity $\epsilon \simeq 0.45$ in Table 9 as compared with $\epsilon \simeq 0.50$ for the outer disk; Davoust et al. 1984; Busarello et al. 1996). Consistent with this, Bureau et al. (2002) and de Zeeuw et al. (2002) find evidence for a "disk embedded in the bulge" (high rotation and a flattened light distribution) from SAURON observations.

5.4. *NGC 3608*

NGC 3608 is a core galaxy in the Leo Group, separated by only $5\rlap{.}'8$ (39 kpc) from NGC 3607. It is undetected at 6 cm (Wrobel & Heeschen 1991) but contains extended X-ray emission [$\log(L/\text{ergs s}^{-1}) = 40.4$; Pelligrini 1999]. Surface photometry shows an E2 elliptical with slightly boxy isophotes beyond $5''$. Nuker law parameter fits are published for the WFPC1 data in Lauer et al. (1995) and Faber et al. (1997), and we tabulate the parameters for the WFPC2 V image in Table 6. NGC 3608 has a definite core profile with $\gamma \approx 0.06$. There is evidence for patchy dust in the WFPC2 data. Carollo et al. (1997) note an elongated dust feature in the innermost $0\rlap{.}''6$ (67 pc for $d = 23$ Mpc) that looks like an off-centered ring. Tomita et al. (2000) estimate the dust feature to be 190 pc across. Singh et al. (1994) suggest that the interacting neighbor, NGC 3607, has acquired gas and dust from NGC 3608.

Our ground-based kinematics (see Fig. 12) can be compared to those in Jedrzejewski & Schechter (1988, 1989). Our mean velocity and velocity dispersion profiles are consistent with those published by these authors, although they plot a few more points beyond $20''$. The outstanding feature of NGC 3608 is the kinematically distinct core. The slope of the rotation curve changes sign at about $5''$ (coincident with the onset of boxy isophotes), and the rotation itself changes sign at $r \approx 13''$. The maximum rotation is only 24 km s^{-1}, giving NGC 3608 the lowest v/σ in our sample. Our STIS velocity dispersion profile shows a central peak that is
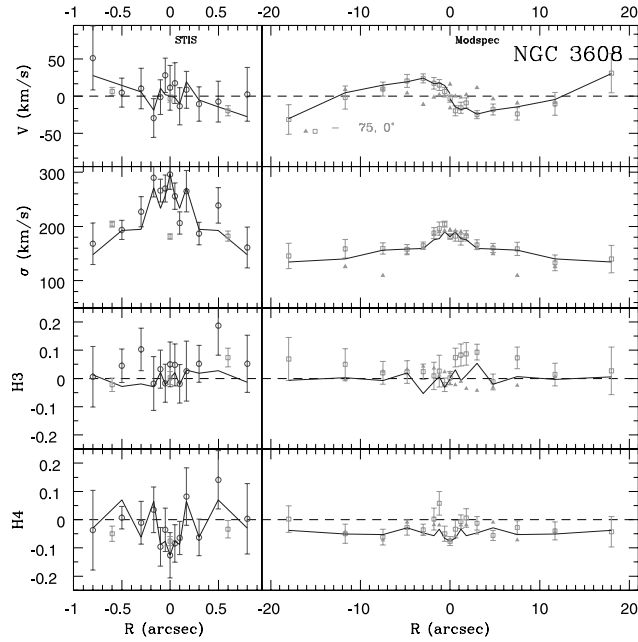
Fig. 12.—Kinematic profiles for NGC 3608 (see Fig. 9 for the meaning of the symbols). For NGC 3608, all ground-based position angles are from Ca spectra. [*See the electronic edition of the Journal for a color version of this figure.*]
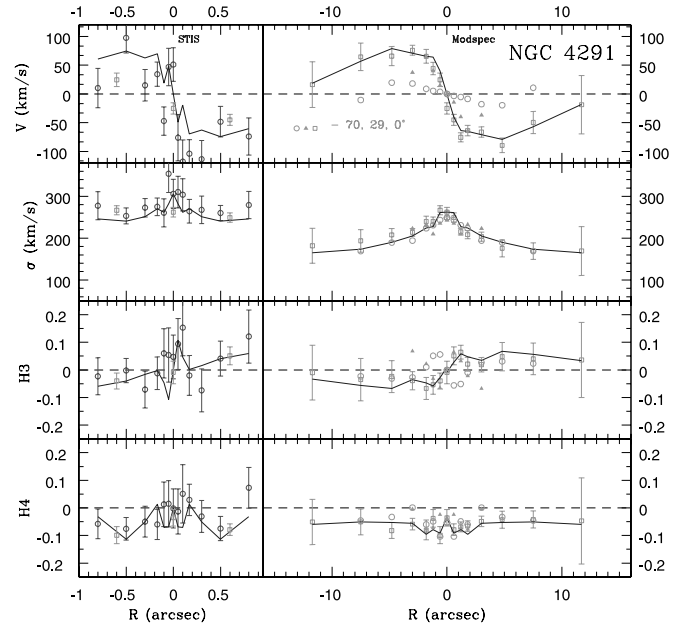

Fig. 13.—Kinematic profiles for NGC 4291 (see Fig. 9 for the meaning of the symbols). For NGC 4291, all ground-based position angles are from Ca spectra. [*See the electronic edition of the Journal for a color version of this figure.*]

higher than the ground-based value by about 100 km s^{-1}. Also notable is the significantly negative central h4 values in the ground-based data.

5.5. *NGC 4291*

NGC 4291 has a low luminosity for a core galaxy, $M_B = -19.6$ mag. Michard & Marchal (1994) suspected a peculiar asymmetric envelope, but it is difficult to distinguish because of nearby stars. It is neighbored by NGC 4319 only 7$.'$4 (56 kpc at $d = 26$ Mpc) away but does not appear to be interacting (RC3). Like other core galaxies, it has slightly boxy isophotes ($100a_4/a = -0.3$; BSG94) and an excess of X-ray emission above that expected from binary stars alone (Pellegrini 1999).

Our STIS light profile for NGC 4291 (Fig. 6) shows a slight excess at $r < 0$.''1. No strong evidence exists for a central excess in the light profile of the WFPC2 images.

Our major-axis kinematics for NGC 4291 can be compared to those of BSG94 and Jedrzejewski & Schechter (1989). All data sets show a centrally rising velocity dispersion that peaks at 270–300 km s^{-1} (see Fig. 13). The rotation peaks at $\sim$80 km s^{-1} at about 5$''$ and then declines to about 40 km s^{-1} by 12$''$. This overshoot is reminiscent of disky galaxies like NGC 3384, but there is no photometric evidence for a disk in NGC 4291. The other authors also show minor-axis spectra, whereas we have a spectrum offset by 29°. NGC 4291 shows very little minor-axis rotation (e.g., -3.3 ± 1.2 km s^{-1}; Jedrzejewski & Schechter 1989; BSG94). The velocity profile shows an asymmetric overshoot at $\sim$5$''$ suggestive of a corotating core. We find lower h4 values in our ground-based data than do BSG94. The BH mass estimate from the two-integral modeling of Magorrian et al. (1998) is 1.9×10^9 $M_\odot$, while three-integral modeling applied to the data herein gives 3.1×10^8 $M_\odot$ (Gebhardt et al. 2003). This is the largest such discrepancy in our

sample. We believe that it results from the Magorrian et al. (1998) assumption of isotropy. Wrobel & Herrnstein (2000) observed NGC 4291 in 8.5 GHz and placed an upper limit on its advection-dominated accretion flow (ADAF) accretion rate using the Magorrian et al. (1998) BH mass estimate.

5.6. *NGC 4473*

NGC 4473 is an E5 galaxy in the Virgo Cluster. As seen in other E5 galaxies, the isophotes are primarily disky (Bender et al. 1988; Michard & Marchal 1994). Van den Bosch et al. (1994) note some irregularities in the higher order deviations from ellipses between 2$''$ and 4$''$, but ground-based surface photometry generally reveals an ordinary, disky elliptical.

Some searches for ISM, dust, and emission-line gas have found none (Roberts et al. 1991; Michard & Marchal 1994; Ho, Filippenko, & Sargent 1997), while Macchetto et al. (1996) detect a small amount (1200 $M_\odot$) of excited gas in Hα, and Ferrari et al. (1999) report a similarly sized dust disk at their limit of detection.

Our kinematic measurements are very good for NGC 4473 because of its relatively high surface brightness (see Fig. 6). In particular, the signal in the higher order moments, h3 and h4, is relatively strong (Fig. 14). Our ground-based values of h3 are in good agreement with BSG94, but our h4 and σ values are systematically lower. We find h4 to be negative at most radii and gradually increasing toward the center; h4 then shows a central dip at STIS resolution. Our σ profile shows a gradual decrease toward the center where our ground-based values are about 10 km s^{-1} lower than those of BSG94. However, our central, Modspec dispersion (183 km s^{-1}) agrees with the average of 11 sources in Hypercat, 179 km s^{-1}. Young et al. (1978) published long-slit spectroscopy out to 45$''$. They measure a v_{max} of 60 km s^{-1} and $\sigma = 180$ km s^{-1}. Morton & Chevalier
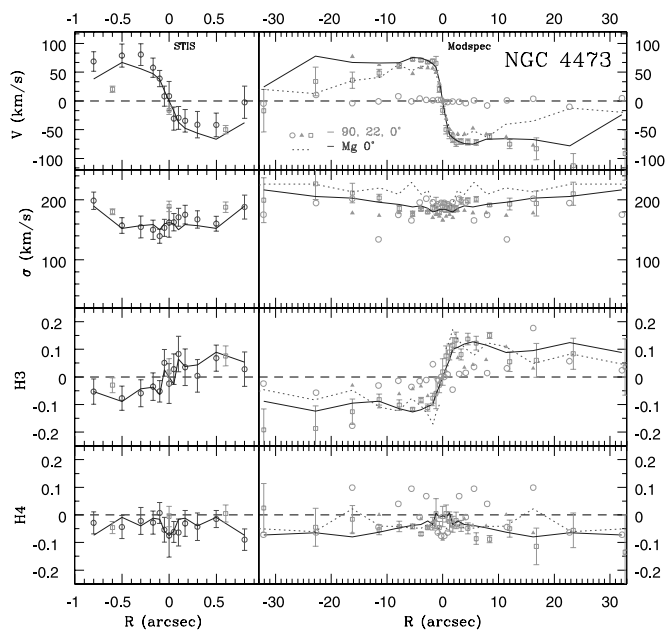
FIG. 14.—Kinematic profiles for NGC 4473 (see Fig. 9 for the meaning of the symbols). For NGC 4473, the dashed line (P.A. = 0°) and the circles (P.A. = 90°) are from Mg spectra. All others are Ca spectra. [*See the electronic edition of the Journal for a color version of this figure.*]

(1973) measured a higher rotation velocity, 100 km s^{-1} at $r = 10''$. Our ground-based v_{max} is 75 km s^{-1}. Michard & Marchal (1994) point out that this rotation is surprisingly small for a disky elliptical.

The high-resolution *HST* imaging reveals NGC 4473 to be an unusual galaxy (see Byun et al. 1996 for WFPC1 results; Table 5 for WFPC2 *V* and *I* results). Its surface brightness profile (Fig. 15) has an asymptotic inner slope, $\gamma = 0.01$ (WFPC2 *I* band, $\gamma = 0.014$ in WFPC1). This makes it a core galaxy by definition ($\gamma < 0.3$; Faber et al.
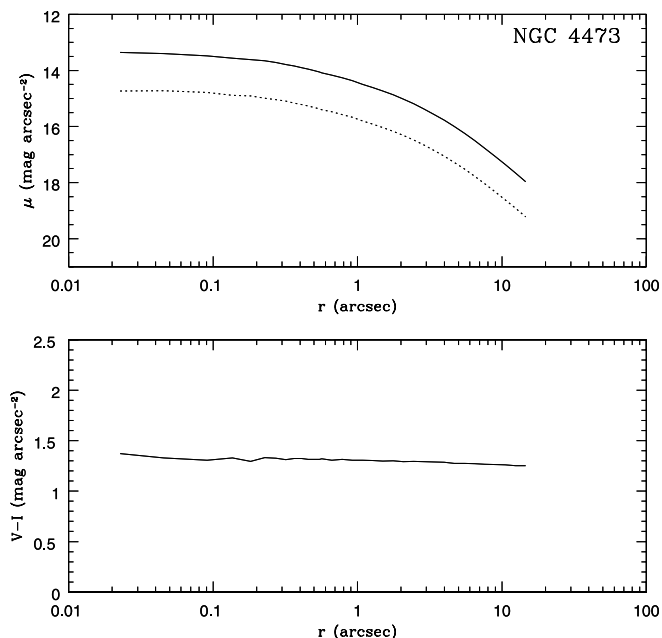
FIG. 15.—*Top:* Deconvolved, WFPC2, *V* and *I* surface brightness profiles of NGC 4473. *Bottom:* (*V*−*I*) color profile.
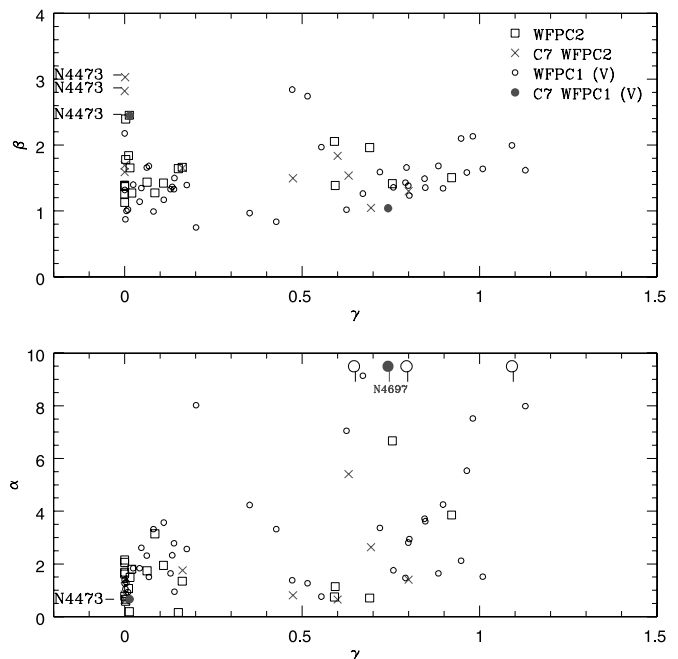
FIG. 16.—Plot of the Nuker law parameters β vs. γ (*top*) and α vs. γ (*bottom*) for 72 galaxies. We chose the *I*-band WFPC2 data whenever possible. The open circles are the WFPC1 data tabulated in Byun et al. (1996). The squares are mostly *I*-band WFPC2 data (*V* or *R* if *I* was not available) from T. R. Lauer (2002, private communication). The crosses and filled circles represent the 10 galaxies of this paper. For NGC 4473 we show three points: WFPC2 *I*, *V*, and WFPC1 *V*. The four galaxies with very large α-values that fall off of the plot are marked by circles with tails. [*See the electronic edition of the Journal for a color version of this figure.*]

1997). However, the transition between the inner and outer slopes is very gradual ($\alpha = 0.66$ for WFPC1; 0.70 for WFPC2), while all the other cores have $\alpha = 1.0$–8.0 (the next smallest being NGC 3608, with the counterrotating core). Furthermore, the outer slope of the profile ($\beta = 2.45$ and 2.7 for WFPC1 and WFPC2 *I* band, respectively) is very steep: it has the highest β among the cores in Byun et al. (1996). Figure 16 demonstrates how NGC 4473 has unusual Nuker parameters. Finally, the absolute magnitude, $M_B \sim -19.9$ mag, is consistent with power-law galaxies, falling faintward of the region of overlap between power laws and cores (Faber et al. 1997). Why does a relatively faint, E5, disky elliptical have the central profile of a core galaxy?

A recent merger can provide several explanations for these peculiarities. First, the merger could contribute a secondary nucleus that could artificially flatten the inner surface brightness profile and account for the gradual transition between the inner and outer slopes. Second, the merger could deposit dust that masks the central surface brightness peak. Third, the merger may be accompanied by an inflow of gas that forms into a stellar disk or torus that, in turn, makes the original peak less distinct.

There is some evidence for each of these scenarios. For example, a disky stellar structure at $r < 2''0$ is suggested by the increasing ellipticity of isophotes toward the center; WFPC1 surface photometry shows isophotes increasing in ellipticity from 0.36 at 15$''$ to 0.5 at 0$''$5 (van den Bosch et al. 1994). Evidence for the *recent* formation of a stellar disk includes the blue color of the stellar disk detected in ground-based images (Goudfrooij et al. 1994b). The presence of dust

is supported by the aforementioned observation of central dust and gas (Ferrari et al. 1999). Finally, in support of double nuclei or tori, Byun et al. (1996) noted "double nucleus?" for NGC 4473 in their Table 1. Perhaps it is no coincidence that NGC 4473 also shows the most conspicuous asymmetry in its STIS light profile for our entire sample: a shoulder located $\approx 0\rlap{.}''2$ from the peak (see § 4.5, Fig. 6).

The above conclusions that dust, blue colors, and secondary nuclei are present are all based on only marginal detections. Thus, we have inspected the deconvolved *HST* WFPC2 images for corroborating evidence. The *I*- and *V*-band images (Fig. 17) have 2000 and 1800 s total exposure, respectively. They provide higher resolution than the WFPC1 data used by van den Bosch et al. (1994). Our *HST* ($V-I$) color profile in Figure 15 does not confirm the blue color of the disk, although blue and red light may be mixed within each elliptical isophote. A double nucleus is not present in the form of two, distinct maxima. However, the contours appear compressed along the minor axis so as to make isophotes "peanut" shaped at $r \approx 0\rlap{.}''2$. Ellipse fitting reveals that the strong diskiness in isophotes at $r > 1\rlap{.}''6$ (peaking at $100a_4/a = 2.3 \pm 0.5$ at $r = 4\rlap{.}''3$) suddenly gives way to very strong boxiness at $r < 1\rlap{.}''6$; the $100a_4/a$ drops below -5.0 at $r = 0\rlap{.}''23$ and then returns to values consistent with 0 at the resolution limit ($r \approx 0\rlap{.}''1$). The noisiness of the deconvolution process should be taken into consideration; the peak pixel is not in the same position in the two bottom images and the minimally smoothed contours are noisy. However, the position of the boxiest isophotes is robust, occurring at $r \approx 0\rlap{.}''2$ in both the *V*- and *I*-band deconvolved images and reaching magnitudes as low as $100a_4/a = -5$ in

both data sets. The top panels of Figure 17 show that subtracting a purely elliptical model leaves behind an X-shaped residual in both cases. The offset of the peak residual from the best-fit ellipse centroids is also robust, suggesting an asymmetric enhancement about $0\rlap{.}''1$ from those centroids. At $r > 1''$ (not shown), the residual pattern inverts to a dark "+," indicating the diskiness previously reported by others.

The asymmetry we see in the residuals after subtracting an elliptical model is one way to explain the shoulder in the light profile along the STIS slit. A more direct test is to simulate the STIS slit aperture on the WFPC2 data and create light profiles. These profiles are shown in Figure 6. The light is more concentrated near the center because of the greater spatial resolution in the WFPC2 data, especially in the deconvolved data. Nevertheless, the profiles are higher to the right of the center than to the left under the "double nucleus" label.

Figure 18 is an overlay of the $0\rlap{.}''2$ STIS slit onto the *V*-band WFPC2 image. Notice that the STIS slit is skewed with respect to the major axis by $20°$, more than any other galaxy in our sample (this was necessary to acquire the guide stars). Nevertheless, the position of the slit allows the passage of some light from the region that created the X-shaped residuals.

There are no obvious signs of a recent merger in the kinematics. No counterrotation is seen in the velocity profile, and the velocity overshoot seen at $5''$ is typical of elliptical galaxies with embedded disks. The photometry and STIS light profile (Fig. 6) suggest a possible secondary nucleus at $r \approx 0\rlap{.}''2$, so a kinematic deviation might be expected at STIS resolution. The unsymmetrized STIS dispersion in
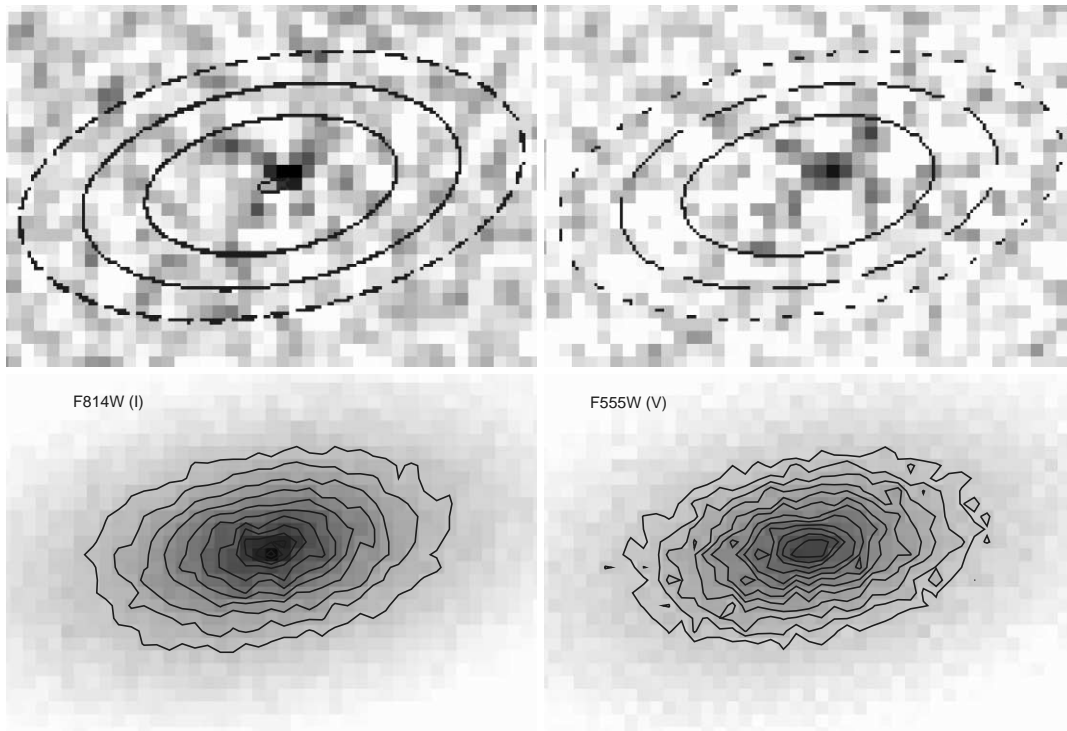

Fig. 17.—WFPC2 gray-scale images of the inner part ($r < 0\rlap{.}''7$) of NGC 4473. Dark gray levels represent large pixel values in all panels. *Top: I*-band (*left*) and *V*-band (*right*) residuals after subtraction of a model with purely elliptical isophotes. Some isophotes from the ellipse fitting are shown. The center was a free parameter. *Bottom: I*-band (*left*) and *V*-band (*right*) images before model subtraction, displayed with the same orientation and scale. Each has 40 iterations of Lucy-Richardson deconvolution. Minimally smoothed contours are overlaid with linearly spaced levels. The inner isophotes become so boxy as to appear peanut shaped.
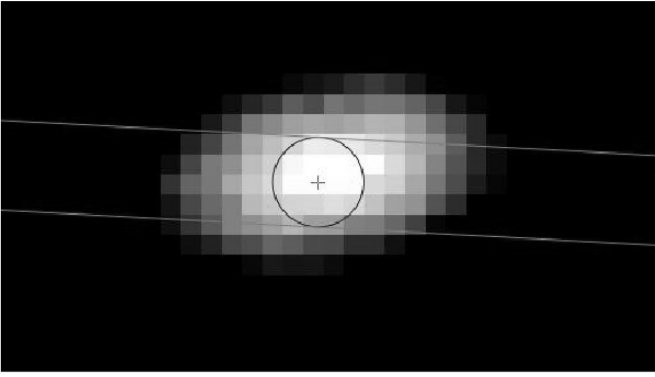
FIG. 18.—V-band WFPC2 data shown with the STIS slit overlayed to match the observation. The circle is $0\rlap{.}''2$ wide. North is $173°$ clockwise from up, and the position along the slit used elsewhere in this paper increases toward the left.

Figures 14 and 7 does, in fact, show a smooth gradient across the center, but it is only marginally significant. NGC 4473, like NGC 3384, has a lower central dispersion in the STIS data than in the ground-based data, indicating a kinematically cold stellar population near the center. These two galaxies are interesting to contrast: both show kinematic and photometric evidence for a cold stellar disk all the way into the center, yet NGC 4473 has much lower (v/σ) than NGC 3384. Moreover, NGC 4473 has a core profile with an indistinct center, while NGC 3384 has a power-law profile with the strongest central peak in our sample.

We conclude that NGC 4473 is a peculiarity—a disky galaxy lacking a strong central cusp—and that its peculiarities probably originated with a merger. The occurrence rate of such "disky cores" is low, judging by the study of Rest et al. (2001), which classifies only one of nine cores as "disky" (within a sample of 57 galaxies). Any *obvious* evidence for a recent merger is absent; there is no counterrotating stellar or gas system, no erratic dust, and no multiple nuclei. However, current work on the formation of cores (e.g., Faber et al. 1997; Milosavljević & Merritt 2001; Makino 1997) involves the merger and coalescence of two galactic nuclei with BHs, and these scenarios predict that observability of the merger will diminish continuously. Some cores have been identified with easily resolved double nuclei (e.g., NGC 4486B; Lauer et al. 1996), and recently six cores have been identified with subtle "central inversions" in their surface brightness profile that are likely to be toroidal stellar systems (Lauer et al. 2002). NGC 4473 may be another case of subtle central structures resulting from coalescing binary nuclei. Like most of those in Lauer et al. (2002), it has a poorly defined central peak and peanut-shaped isophotes. NGC 4473 differs in that it has disky isophotes at $r \gtrsim 1''$. Alternatively, no BHs were contributed by the last merger, only gas that has subsequently formed a substantial disk at $r > 1\rlap{.}''5$ and a noncuspy structure (possibly a torus) near the limits of resolution. Future imaging at slightly higher resolution should clarify the central structure.

5.7. NGC 4564

NGC 4564 is classified by Sandage & Tammann (1980) as an E6, but it has characteristics of an S0. First, its isophotes show disky deviations from an ellipse at large radii. The parameter a_4/a begins to climb at $10''$, reaching about 0.025

at $20''$ and then tapering down to 0.01 (Bender et al. 1988). Such diskiness at intermediate radii is also seen in NGC 821. Second, its ellipticity increases gradually from 0.2 at $r = 3''$ to 0.6 at $30''$ (Bender et al. 1988). Sahu, Pandey, & Kembhavi (1996) decompose their R-band image into an elliptical bulge (obeying a de Vaucouleurs law) and a disk. Their scale length for the disk is $r_s = 28\rlap{.}''14$ with axial ratio $b/a = 0.3$. Third, Sil'chenko (1997) finds a younger stellar population in the center of the disk (8 Gyr) compared to the rest of the galaxy.

High-resolution images were obtained with WFPC1 (PID 2607; Byun et al. 1996) and WFPC2 (Jaffe, PID 6357; Faber et al. 1997). In the center, NGC 4564 appears more bulge dominated, with rounder isophotes and boxy deviations from ellipses. For example, van den Bosch et al. (1994) find that the ellipticity is only 0.16 at $0\rlap{.}''5$ and that a_4/a is significantly negative around $2\rlap{.}''0$. They also find sharp variations in P.A. and ϵ near $2\rlap{.}''0$. This is indicative of dust; however, Roberts et al. (1991) do not find evidence for ISM.

Our ground-based kinematics for NGC 4564 (Fig. 19) can be compared to those of BSG94 and Halliday et al. (2001). Our spectra have relatively low S/N (Fig. 3). The published profiles are in good agreement with ours but are plotted to greater radii ($r = 35''$ and $40''$, respectively). The velocity dispersion declines by a factor of 2 from $0''$ to $10''$, so one should expect large variations in published values of σ-dependent quantities. For example, Bender (1988) gives a v_{max}/σ of 1.11 ($v_{max} = 150 \pm 5$ km s^{-1}, $\sigma = 135 \pm 5$ km s^{-1}), while we have 1.3 ± 0.2 ($v_{max} = 147 \pm 4$ km s^{-1}, $\bar{\sigma} = 112 \pm 17$ km s^{-1}; see Table 9). The average of six central velocity dispersions in Hypercat is 158 km s^{-1}, while we measure $\sigma_0 \approx 170$ km s^{-1} in all of our Modspec position angles. Asymmetric (h3) deviations of the LOSVDs from a Gaussian are not significant, but h4 appears to be negative at $r < 10''$. Halliday et al. (2001) show h3 becoming negative beyond $10''$, coincident with an increase of a_4 above 0. The
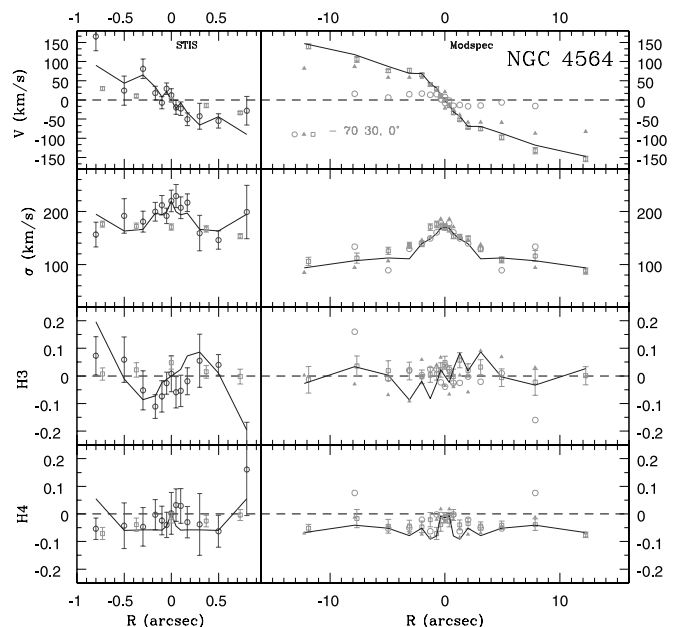

FIG. 19.—Kinematic profiles for NGC 4564 (see Fig. 9 for the meaning of the symbols). For NGC 4564, all ground-based position angles are from Ca spectra. [*See the electronic edition of the Journal for a color version of this figure.*]

sudden changes in the P.A., ellipticity, $\cos 3\theta$, and $\cos 4\theta$ coefficients at $2\rlap{.}''0$ (van den Bosch et al. 1994) are coincident with subtle bends in our profiles of symmetrized v, σ, and h4.

The STIS kinematics features a central velocity dispersion peak of 220 ± 20 km s^{-1}, well above the ground-based result. The higher resolution also reveals rotation of ~ 50 km s^{-1} in the inner $1\rlap{.}''0$. In addition, h3 and h4 are fairly noisy, but the symmetrized curves indicate a gradient in h3 across the inner $0\rlap{.}''5$ and predominantly negative h4. The kinematics allows a secure detection of a BH (Gebhardt et al. 2003), but little evidence for nuclear activity is found in X-rays (Pellegrini 1999) or radio continuum (Wrobel & Herrnstein 2000).

5.8. *NGC 4649*

NGC 4649 (M60) is a giant elliptical in the Virgo Cluster, comparable in luminosity to M87. NGC 4649 stands out in our sample as the galaxy with the lowest central surface brightness (Fig. 6) and highest luminosity. It is the only galaxy with a large enough dispersion so that the crowding of the Ca II triplet absorption lines becomes problematic. This will be discussed further in § 6.

We find a $10^{9.3}$ $M_\odot$ BH in NGC 4649 (Gebhardt et al. 2003), only about 30% less massive than the BH in M87 (Macchetto et al. 1996). Fortunately, it has far weaker nuclear activity than M87, thus simplifying a BH search. Nuclear activity is detected in the radio (Fabbiano et al. 1987) but not in the optical or X-rays (Byun et al. 1996; di Matteo & Fabian 1997). Stanger & Warwick (1986) also find only low-level extended radio emission out to $\sim 3\rlap{.}''0$. Di Matteo & Fabian (1997) estimate that the total measured core flux from radio to X-ray is lower than 10^{41} ergs s^{-1}.

NGC 4649 is separated by only $2\rlap{.}'5$ (~ 12 kpc for a distance of 16 Mpc) from the spiral NGC 4647. Many studies report that they are noninteracting (e.g., Sandage & Bedke 1994), although the spiral is clearly asymmetric (see Koopmann et al. 2001). It is given an E2 morphology by RC3, but Sandage & Bedke (1994) think it is an S0$_1$ because of its "prominent extended envelope." NGC 4649 has an extended X-ray halo (Bohringer et al. 2000), and it has been identified with its own compact subgroup within the Virgo Cluster (Mamon 1989).

CCD surface photometry has been performed by Peletier et al. (1990), Caon et al. (1990), and Michard & Marchal (1994). There are no significant deviations from ellipses in the isophotes between $1''$ and $8''$, and then they become mildly boxy ($100a_4/a \approx -0.5$). The maximum ellipticity measured by Peletier et al. (1990) is ≈ 0.2, which suggests a nearly face-on inclination ($i < 36°$). This makes difficult the detection of disky isophotes (Michard & Marchal 1994). Instead, support for the S0 classification is found in the surface brightness profiles, which show an outer envelope above the $r^{1/4}$-law bulge. There is no strong evidence for a tidal influence from nearby NGC 4647. *HST* WFPC2 *V*-band photometry is discussed by Byun et al. (1996) and Faber et al. (1997). NGC 4649 has a core profile with a break radius of $3\rlap{.}''58$.

Our ground-based kinematics (Fig. 20) can be compared to those of Fisher et al. (1995), de Bruyne et al. (2001), and BSG94. Fisher et al. (1995) report an average rotation of 87 km s^{-1}, and their rotation curve climbs from 60 to 120 km s^{-1} between $r = 20''$ and $60''$. Similarly, our rotation curve is
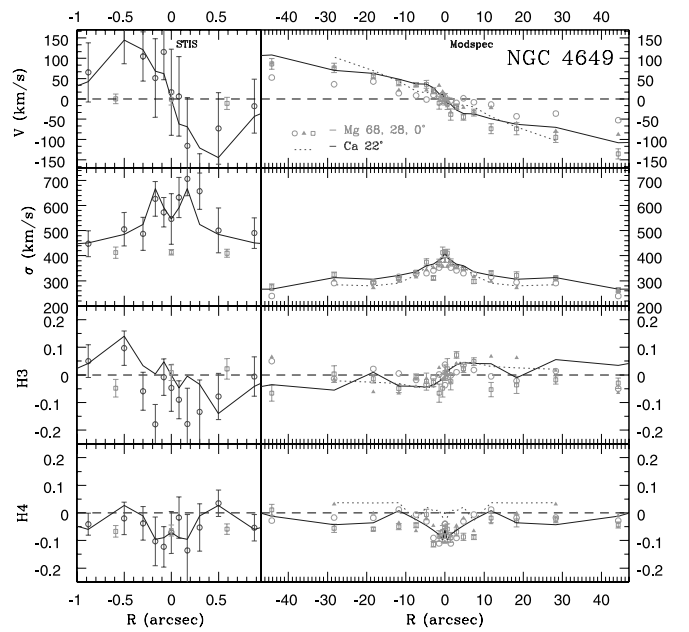

FIG. 20.—Kinematic profiles for NGC 4649 (see Fig. 9 for the meaning of the symbols). For NGC 4649, all of the ground-based data are from Mg spectra except the dashed line (P.A. $= 22°$), which is Ca spectra. [*See the electronic edition of the Journal for a color version of this figure.*]

climbing at $45''$ where it is ~ 110 km s^{-1} (symmetrized). In general, NGC 4649 has strong rotational support compared to other giant elliptical galaxies. Its large $(v/\sigma)^*$ stands apart from the brightest cluster galaxies in the study of Fisher et al. (1995). Our unsymmetrized rotation curve is also fairly *asymmetric* with respect to the galaxy center. The data of de Bruyne et al. (2001) demonstrate this even better with a rotation curve out to $90''$, showing an ~ 70 km s^{-1} maximum difference in rotation between the two sides. This asymmetry along the major axis provides some support for the idea of an interaction with NGC 4647.

Our velocity dispersion profile is consistent with that of BSG94 and de Bruyne et al. (2001), but Fisher et al. (1995) have systematically lower values. Most dispersion profiles peak at ~ 400 km s^{-1} and then rapidly decline to ~ 300 km s^{-1} by $r = 20''$; they show nearly a factor of 2 decrease from the center to the effective radius ($r_e \approx 80''$). De Bruyne measures positive h4 values within $10''$, whereas we measure negative h4 here at all of our position angles.

The STIS Ca II triplet data reveal an enormous central velocity dispersion. The entire inner $1\rlap{.}''0$ is above 450 km s^{-1}, and it appears to rise to over 600 km s^{-1}. However, the uncertainties are high because of the ill-defined absorption lines (§ 6). This differs from the case of IC 1459 (Cappellari et al. 2002), another giant elliptical ($M_B \approx -21.4$), which has $\sigma_0 \approx 350$ km s^{-1} in both STIS and ground-based observations. Another unusual (but uncertain) feature is the strong rotation within $1\rlap{.}''0$. The maximum STIS rotation, ~ 150 km s^{-1}, exceeds the maximum ground-based rotation.

5.9. *NGC 4697*

This is an E6 galaxy with a stellar disk along the apparent major axis (Carter 1987; Goudfrooij et al. 1994b). NGC 4697 has more dust and gas than the other galaxies in this sample. Molecular gas was detected by Sofue & Wakamatsu (1993), and the high *IRAS* 100 μm flux densities also imply

cool gas. The radial color gradient is larger than the metal-licity gradient from the Mg_2 index (Peletier et al. 1990). *HST* WFPC1 imaging reveals an organized dust disk (Lauer et al. 1995). This dust was not successfully imaged from the ground (Véron-Cetty & Véron 1988; Kim 1989) but was suggested by the red nucleus in $B-I$ (Goudfrooij et al. 1994b). The $H\alpha + [N\ II]$ emission proved difficult to detect (Trinchieri & di Serego Alighieri 1991; Kim 1989). Long-slit spectroscopy by Goudfrooij et al. (1994a) gives an $H\alpha + [N\ II]$ flux of 2.4×10^{-13} ergs s^{-1} cm^{-2}. The narrow-band imaging by these authors shows $H\alpha + [N\ II]$ emission extending out to $35''$. Ground-based imaging (e.g., Peletier et al. 1990) indicates embedded, disky isophotes. The parameter $100a_4/a$ is over 1.8 until $r = 20''$, and then it declines to 0.

A great deal of spectroscopy exists for comparison with our Modspec results. Bertola & Capaccioli (1975) first pointed out that elliptical galaxies are not rotationally supported using NGC 4697. It has also been used for case studies showing that three-integral models are an improvement over two-integral models (Dejonghe et al. 1996; Binney et al. 1990).

Carter (1987) points out that there is a large variation in v_{max} measurements for this galaxy. Bertola & Capaccioli (1975) find 65 km s^{-1}, Illingworth (1977) gets 90 km s^{-1}, and Davies (1981) derives 146 km s^{-1}. We measure a ground-based $v_{max} = 101 \pm 13$ and an STIS v_{max} of 110 ± 21 km s^{-1}. A likely explanation is the presence of a cold, rapidly rotating, stellar disk (composing more than 10% of the light along the major axis), which has a varying effect on the measured radial velocity for different methods. Figure 21 includes the rotation curve of the excited gas (*filled circles*) measured from [N II] emission with STIS (J. Pinkney et al. 2003, in preparation). This provides an interesting contrast to the stars in that the gas shows less pressure support beyond $0''.2$.

The mean central velocity dispersion given by Hypercat is 174 km s^{-1}. This is a bit higher than our central, ground-based, velocity dispersions of 157, 159, and 164 km s^{-1}, for our $0°$, $48°$, and $70°$ slit orientations, respectively. We measure a higher central dispersion with STIS, 171 km s^{-1}. This galaxy stands out as one of the few with a local minimum at $r = 0$ in the STIS velocity dispersion profile (Fig. 21). It is also unusual in that its h4 parameter is significantly positive (see § 6.3).

5.10. *NGC 7457*

NGC 7457 is the smallest, lowest luminosity galaxy in our sample. It is an S0 galaxy, like NGC 3384. NGC 7457 is another example of a *pseudobulge* (see § 5.3) in our sample, based on photometry and kinematics (Fig. 22). Tomita et al. (2000) find a pointlike, bluish nucleus in the WFPC2 (V, I) data, and Peletier et al. (1990) find a young stellar population in the bulge. Michard & Marchal (1994) detect a small bar.

Lauer et al. (1991) report on the WFPC surface brightness profile and find it unresolved and steep. The improved *HST* WFPC2 imaging reveals a surface brightness profile with a very shallow outer power law; its $\beta = 1.05$ (T. R. Lauer 2002, private communication) is the smallest in a sample of 29 early-type galaxies. However, the surface brightness profile in Andredakis, Peletier, & Balcells (1995) has a Sersic parameter $n \approx 6.2$, which is higher than the values $n \lesssim 2.0$ more typical of pseudobulges. Most impressive is the strong surface brightness peak in deconvolved WFPC2 F555W data (T. R. Lauer 2002, private communication), which jumps 4 mag in the inner $0''.1$. Tomita et al. (2000) do not interpret this as an AGN because of the lack of $H\alpha$ and $H\beta$ emission reported by Ho et al. (1997). However, Gebhardt et al. (2003) find a central drop in calcium triplet equivalent widths and interpret the peak as AGN light.
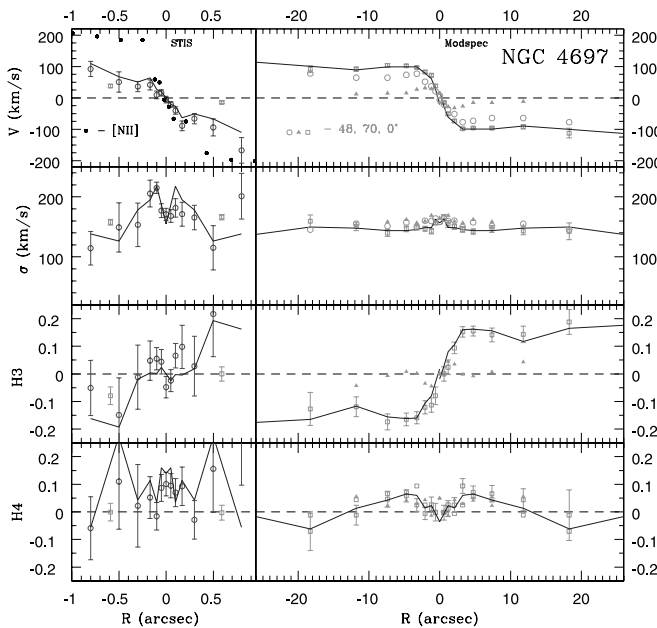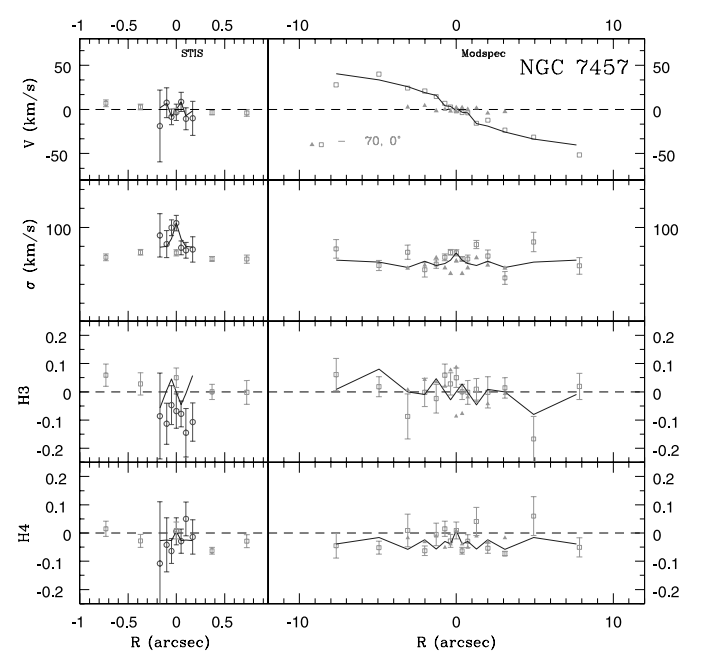

FIG. 21.—Kinematic profiles for NGC 4697 (see Fig. 9 for the meaning of the symbols). For NGC 4697, all ground-based position angles are from Ca spectra. In the top left-hand panel, we include filled circles for [N II] emission line kinematics (see J. Pinkney et al. 2003, in preparation). [*See the electronic edition of the Journal for a color version of this figure.*]

FIG. 22.—Kinematic profiles for NGC 7457 (see Fig. 9 for the meaning of the symbols). For NGC 7457, all ground-based position angles are from Ca spectra. [*See the electronic edition of the Journal for a color version of this figure.*]
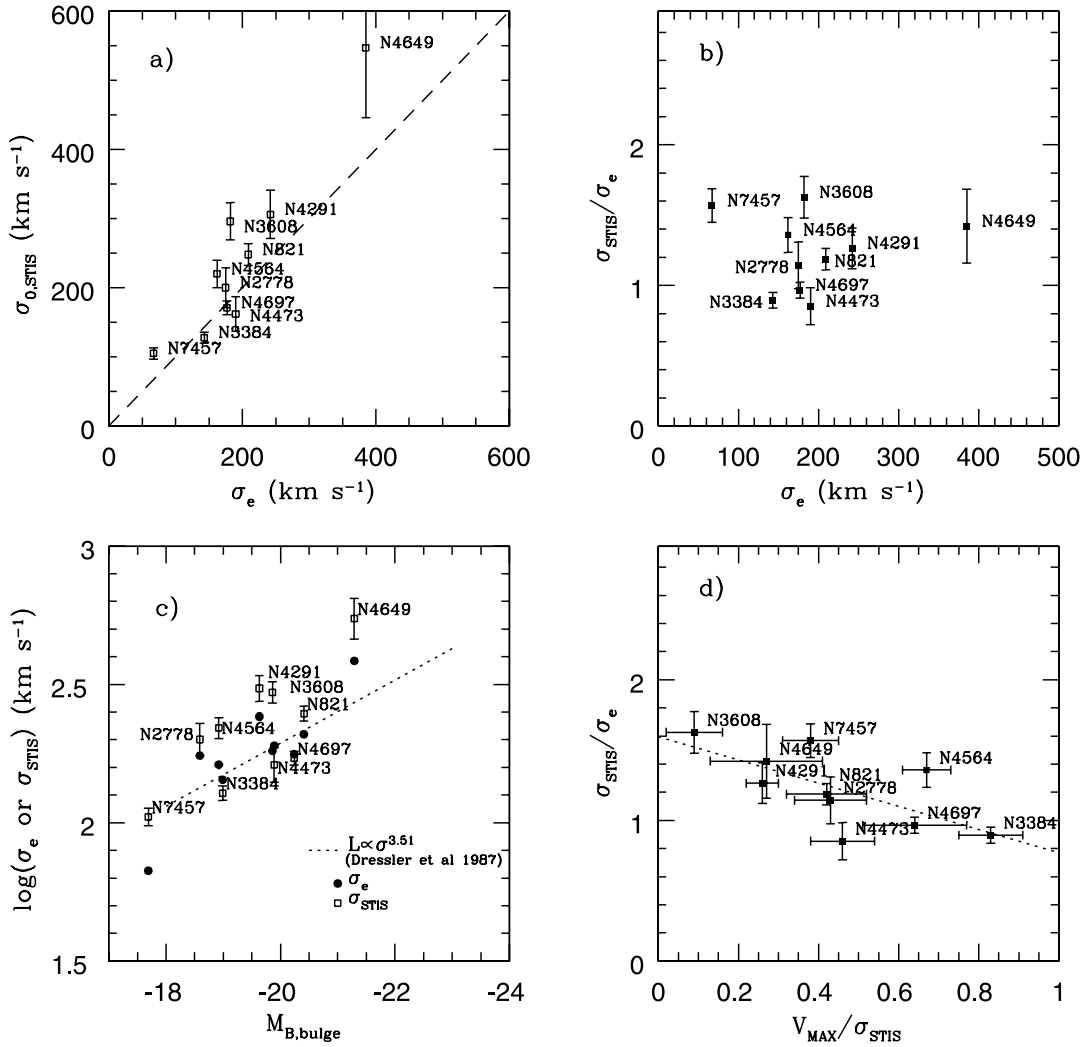
FIG. 23.—Comparisons of high- and low-resolution velocity dispersion measurements for our 10 target galaxies. (*a*) Velocity dispersion measured in the central STIS bin vs. the effective velocity dispersion (a luminosity-weighted dispersion from Modspec data). (*b*) Ratio of central STIS dispersion to the effective dispersion vs. effective velocity dispersion. (*c*) Faber-Jackson relation for our ground-based dispersion, σ_e (*filled circles*), and our central STIS dispersion, σ_{STIS} *open circles*). The best-fit relation from Dressler et al. (1987) is shown as a dashed line. (*d*) Ratio of the centrally measured STIS velocity dispersion to the effective dispersion, σ_e, vs. the maximum ground-based rotation divided by σ_{STIS}.

We find evidence for pseudobulge-like kinematics for NGC 7457. Our Figure 23 demonstrates that the velocity dispersion falls low on the Faber-Jackson relation. This result is robust for different global values of σ from Table 9. Our v_{max}/σ values (Table 9) are not especially large, however, given the ellipticity.

6. DISCUSSION

6.1. *Central Velocity Dispersions*

To what extent does the STIS central velocity dispersion drive the detection of the nuclear black holes? Modeling is required to fully answer this question; however, a strong peak in dispersion in the central $0\rlap{.}''5$ ($\sim$45 pc at $d = 17$ Mpc) is difficult to explain without a central dark mass (van der Marel 1994a). In Figure 23 we compare the central STIS dispersion to our ground-based, "effective" dispersion, σ_e (i.e., the rms velocity relative to the systemic velocity of the galaxy, averaged over a slit width of $1''$ extending to R_e; G00). In seven out of 10 cases, the STIS central value is

higher. The most extreme differences are NGC 4649 (162 km s^{-1}, 42%), NGC 3608 (114 km s^{-1}, 55%), NGC 4564 (58 km s^{-1}, 37%), NGC 4291 (64 km s^{-1}, 17%), and NGC 7457 (38 km s^{-1}, 60%). Three of these have core profiles, and it appears that the core galaxies show the largest differences. NGC 7457 has a 60% increase from σ_e to σ_{STIS}, the greatest fractional rise in the entire sample. Figure 23b demonstrates that the fractional increase does not correlate with increasing dispersion. Likewise, there is no correlation with $M_{B,bulge}$ (not shown). NGC 4473, unlike the other core galaxies, has a σ_{STIS} lower than σ_e. This adds to the growing list of differences between NGC 4473 and the cores (§ 5.6). The other galaxies with lower σ_{STIS} are NGC 3384 and NGC 4697, which are also disky. However, NGC 4697 has a higher σ_{STIS} than our alternative ground-based dispersions $\sigma_{0,GB}$ and $\bar{\sigma}$ in Table 9. Eight of our galaxies, including NGC 3384, show a local maximum at $r = 0\rlap{.}''0$ in their STIS dispersion profile. NGC 4473 shows only a slight central, local maximum, while NGC 4649 and NGC 4697 show local minima in their symmetrized σ profiles. Thus, the majority of galaxies (70%–80%) show a central peak at STIS

resolution, and about 70% have a larger $\sigma_{0,\text{STIS}}$ than σ_e. Only one galaxy, NGC 4697, does not obey either criterion.

In Figure 23c we show the Faber-Jackson (1976) relation for our 10 galaxies. The σ_e is an adequate surrogate for the traditional central dispersions measured through $\sim 2'' \times 2''$ apertures, but use of σ_{STIS} adds scatter to the relation presumably because of the strong dispersion gradient induced by the central black hole. We also find a marginal correlation between the ratio $\sigma_{\text{STIS}}/\sigma_e$ and the ratio $v_{\text{max}}/\bar{\sigma}$, where v_{max} is the maximum rotation in the ground-based data and $\bar{\sigma}$ is the average dispersion in Table 9. Apparently, galaxies with more rotational support have less of a dispersion peak at STIS resolution. The probability that no correlation exists is less than 3% (using Cox regression and Kendall's tau; Isobe, Feigelson, & Nelson 1986) This correlation is present but not as strong if $v_{\text{max}}/\bar{\sigma}$ is replaced by $(v_{\text{max}}/\bar{\sigma})^*$.

6.2. *Low Surface Brightness Giant: NGC 4649*

The galaxies in the BH literature, including our own sample, show a preference for high surface brightness in core galaxies since these are easier to observe. In fact, the measurement of dispersion profiles in core galaxies is so difficult that most of the BH detections in these galaxies rely on emission lines from rotating gas disks (e.g., M87, Harms et al. 1994; NGC 4261, Ferrarese, Ford, & Jaffe 1996; M84, Bower et al. 1998). In the case of the giant E3, IC 1459, Cappellari et al. (2002) have measured the BH mass using stellar kinematics and gas kinematics. However, this galaxy does not have an especially faint surface brightness, $\mu_{V,0''1} \simeq 15.3$ (Carollo et al. 1997). Ground-based stellar kinematics has provided a BH mass estimate for M87 (Dressler & Richstone 1990; van der Marel 1994b), but the BH was not required to fit these data. The preference for high surface brightness cores could conceivably introduce a bias in plots of M_{BH}-σ or M_{BH}-L_B. Moreover, the measurement of BH mass using gas kinematics gives a different answer than stellar kinematics in the only giant where they have been compared (IC 1459; Cappellari et al. 2002). Thus, NGC 4649 is important as the only BH measurement from stellar kinematics in a galaxy that is representative of low surface brightness cores.

Not surprisingly, we find that the LOSVD is particularly difficult to measure in NGC 4649. We requested sufficient exposure time to measure Ca lines in a galaxy with $\mu_{V,0''1} = 15.9$ mag arcsec^{-2} and $\sigma \approx 350$ km s^{-1}. However, this galaxy appears to have a *very* large central velocity dispersion at STIS resolution. This broadens the lines to such an extent that their detection is difficult even at this S/N (Fig. 24). Our MPL technique was able to measure an LOSVD with $\sigma > 500$ km s^{-1}. Naturally, the upper limits are more weakly constrained than the lower limits. The FCQ technique gave more erratic results (not shown in Fig. 20) for these data.

6.3. *Gauss-Hermite Parameters*

Our parameterized stellar LOSVDs suggest properties of a galaxy's orbital structure that are elucidated by the three-integral modeling. This merits a comparison between the two.

Gebhardt et al. (2003) find the tangential component of the velocity dispersion tensor to be stronger in the central bins of the galaxy than in the bins near $R_e/4$ (see Fig. 25b). The h4 parameter also indicates a tangential bias when it
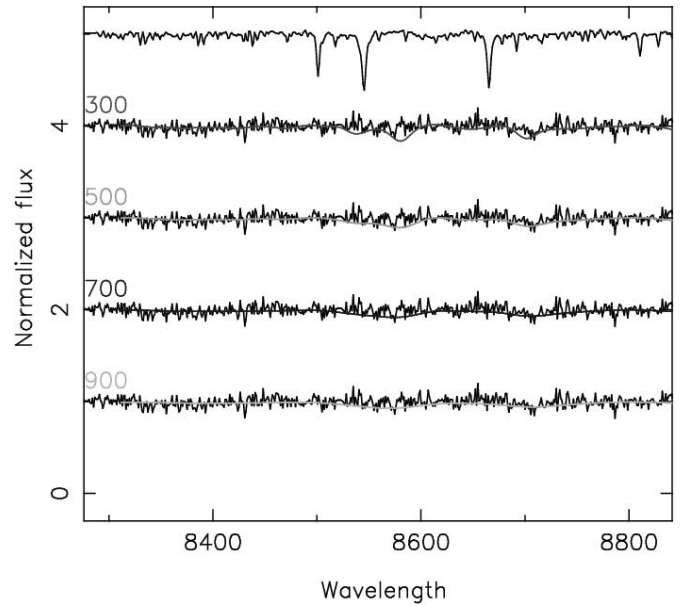

FIG. 24.—Broadened template spectra overlaid on the central, STIS spectrum for NGC 4649. The unbroadened template (HR 6770) is shown on top. It is convolved with progressively broader functions with $\sigma = 300$, 500, 700, and 900 km s^{-1} and then redshifted to 1110 km s^{-1}.

takes a negative value (i.e., the LOSVD is boxy). Indeed, we find that our ground-based h4 profiles usually have a central dip (NGC 821 is a good example). Moreover, the central, STIS-measured h4 parameters, although noisier, are also predominantly negative. To measure a more reliable central STIS h4, we averaged the h4 values from the innermost three bins. Figure 25 demonstrates that these values of h4 are negative in nine out of 10 cases. Individual cases are not significantly negative, but altogether they suggest a real trend. NGC 4473 and NGC 3608 are the most significantly negative. There is one outlier, NGC 4697, which has a positive h4, and this pulls the weighted mean to -0.027 ± 0.01. When this point is excluded, the weighted mean is -0.05 ± 0.01. We looked for correlations between the central h4 value and other photometric and kinematic parameters. The large uncertainties in the h4 values and the small sample do not permit any significant results. A positive correlation is hinted at by Figures 25a and 25c.

It is puzzling that the disky elliptical, NGC 4697, shows positive central h4 values while the other disky galaxies (NGC 821, NGC 3384, NGC 4564, and NGC 4473) have negative central h4 values. One might search for other ways in which NGC 4697 differs from the other four. The most obvious difference is its prominent dust disk at $r < 3''5$. This disk is inclined at $77°$ and has a sharp outer cutoff and a less clear-cut inner radius (J. Pinkney et al. 2003, in preparation). One would expect the same LOSVD regardless of the presence of the dust disk, if the dust disk is an infinitely thin screen centered within an axisymmetric galaxy. However, one could invoke a disk with finite thickness to preferentially obscure, say, an equatorial cold disk component and thereby influence the LOSVDs. A second possible scapegoat is the stellar disk itself, which may be more (or less) prominent in the central STIS bins of NGC 4697 than the other four disky galaxies. One expects a superposition of two LOSVDs with the same centroid but different widths to produce an LOSVD with positive h4. Thus, we may find
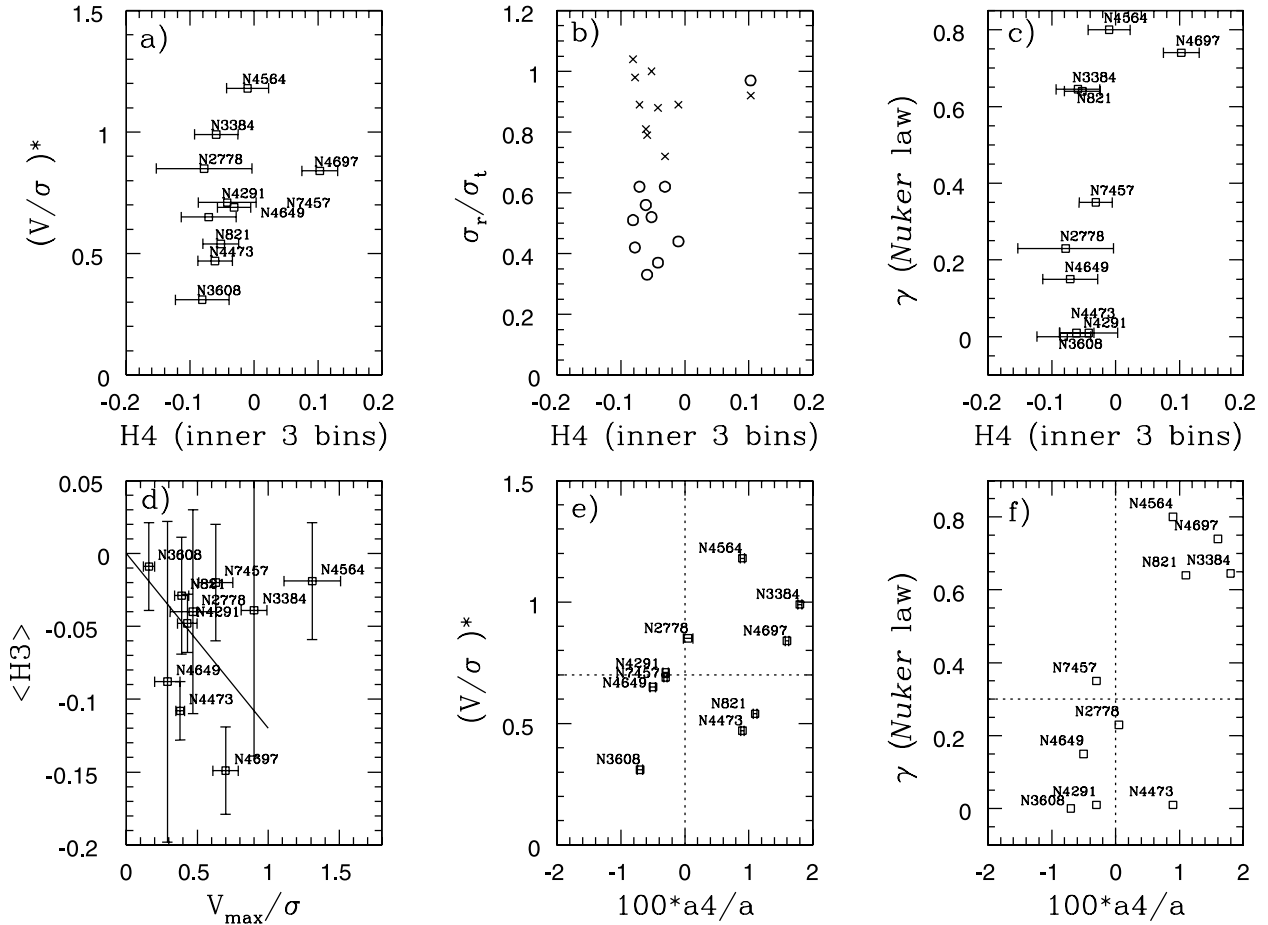
Fig. 25.—Plots of kinematic and structural parameters. (*a*) Anisotropy parameter $(v/\sigma)^*$ vs. h4 averaged over the innermost three STIS bins. The $(v/\sigma)^*$ is calculated using $(v_{max}/\bar{\sigma})/\sqrt{\epsilon/(1-\epsilon)}$, where v_{max} and $\bar{\sigma}$ are taken from Table 9. (*b*) Ratio of the radial to tangential velocity dispersion taken from the modeling by Gebhardt et al. (2003a), σ_r/σ_t, vs. h4 from the innermost three STIS bins. The circles have σ_r/σ_t measured in the central modeling bin, while the crosses were measured at $R_e/4$ (see Gebhardt et al. 2003a). (*c*) Asymptotic power-law slope of the surface brightness profile, γ, vs. h4. (*d*) Mean h3 over $r > 2\farcs0$ of the symmetrized, Modspec data vs. v_{max}/σ. The solid line is the mean relation found by BSG94. (*e*) Ground-based anisotropy vs. $100a_4/a$, the deviations of isophotes from perfect ellipses (taken from the literature). Disky galaxies have $100a_4/a > 0$. (*f*) Asymptotic power-law slope, γ, vs. $100a_4/a$.

positive values of h4 in galaxies where a bulge and disk population overlap. However, there is little evidence in ground-based kinematics that NGC 4697 has a significantly different disk contribution than the other galaxies. In fact, NGC 4473 seems to have the strongest contribution of light from a stellar disk at $r < 5''$: it was the only galaxy that warranted the inclusion of a disk component in the modeling (Gebhardt et al. 2003). Finally, we see in Figure 25 that NGC 4697 has the lowest mean h3 at $r > 2''$ of the entire sample. This is another artifact of diskiness or, more correctly, of strong rotation. Unfortunately, the kinematic properties measured at $r \gtrsim 1\farcs0$ do not necessarily predict the properties at $r \lesssim 0\farcs1$ where the h4 values in question are measured.

The bottom three panels of Figure 25 complement the investigation of GH parameters. First, Figure 25*d* shows our 10 galaxies plotted on a correlation found by BSG94. Our galaxies do not follow the trend well, but this is mostly because of NGC 4564. The v_{max}/σ in this figure uses $\bar{\sigma}$, but if we used $\sigma_{0,GB}$ or σ_e (Table 9), v_{max}/σ would be 0.9 for NGC 4564 instead of 1.3. NGC 4564 happens to have the most extreme variation between $\bar{\sigma}$ and our other two ground-based σ estimates for reasons that are clear in Figure 19. Second, Figure 25*e* demonstrates that galaxies with strong rotational support tend to be disky. This has been estab-

lished with larger samples by BSG94. Third, Figure 25*f* shows a correlation between the asymptotic inner slope γ of the best-fit *Nuker* law surface brightness profile and the deviations of isophotes from ellipses. This follows from the results of, e.g., Faber et al. (1997), wherein the disky galaxies ($100a_4/a > 0$) tend to have power-law profiles and the boxy isophote galaxies ($100a_4/a < 0$) tend to have core profiles. This figure is intended to underscore the peculiarity of NGC 4473 as a "disky core."

6.4. *Demographic Results*

Our sample of early-type galaxies includes a wide range of velocity dispersions (70–385 km s^{-1}) and BH masses ($10^{6.5}$–$10^{9.3}$ $M_\odot$), allowing us to address questions of BH demographics (§ 1). A word should be said about selection effects near the high-mass end of the M_{BH}-σ relationship. The measurement of LOSVDs becomes increasingly more time consuming with decreasing surface brightness. Therefore, a selection bias is introduced whereby, given two core galaxies of the same luminosity or the same dispersion, one is compelled to select the one with the higher surface brightness. We selected one challenging galaxy located in this region of parameter space, NGC 4649, with $\mu_{0,V} = 15.9$ mag arcsec^{-2}. Nevertheless, none of our cores, including

NGC 4649, represent the lowest surface brightnesses known in their luminosity range. It is not certain whether the lowest surface brightness galaxies obey the same demographic trends.

With the discovery of the $M_{\rm BH}$-σ relation, it is natural to look for exceptions to the rule. It appears that the relation holds for Sa and Sb galaxies with classical bulges and even later types (Sc–Sd) with pseudobulges (Kormendy et al. 2003). The Sc galaxy M33 appears exceptional in that it has a BH mass upper limit significantly lower than that predicted using the dispersion of its nuclear star cluster (Gebhardt et al. 2001). This galaxy, however, lacks a hot spheroidal component and so it is debatable whether the $M_{\rm BH}$-σ relation is applicable.

In Figure 26, our 10 BH masses are plotted against velocity dispersion. For just these galaxies, we fit an $M_{\rm BH}$-σ relation of the form

$$\log_{10}\left(\frac{M_{\rm BH}}{M_\odot}\right) = \alpha + \beta \log_{10}\left(\frac{\sigma_e}{200 \text{ km s}^{-1}}\right). \quad (3)$$

The fitting procedure is identical to the one advocated by Tremaine et al. (2002), where we have assumed 5% error in σ_e, and the uncertainty in $M_{\rm BH}$ is the measured one combined with an extra 0.34 dex of intrinsic dispersion, which gives a χ^2 per degree of freedom of unity. We find $\alpha = 8.06 \pm 0.13$ and $\beta = 3.67 \pm 0.70$. Note that the BH masses for the galaxies used in this fit have been refined since G00. All galaxy distances are now taken from Tonry et al. (2001), and more dynamical models have been run to better probe χ^2 space (Gebhardt et al. 2003). Nevertheless, the best fit is nearly indistinguishable from the G00 fit. All of

these same refinements to our sample are incorporated into the preferred fit by Tremaine et al. (2002), which includes an additional 21 galaxies from the literature. The most deviant point is for NGC 2778. This faint galaxy has a lower S/N than most. Furthermore, its sphere of influence is unresolved. Consequently, NGC 2778 has the least confident BH detection when modeled (Gebhardt et al. 2003).

In hierarchical scenarios, the formation of bulges involves mergers that are believed to have occurred during the first few gigayears of the universe. But what is the effect of a merger occurring $\lesssim 1$ Gyr before the present? Will the likely increase in bulge dispersion be accompanied by the appropriate increase in BH mass? We have inspected our galaxies for merger candidates to see if they are systematically displaced on the $M_{\rm BH}$-σ relation. Three of our galaxies show marginal evidence for recent mergers: NGC 3608, NGC 4473, and NGC 4697. NGC 3608 has a counterrotating core and patchy dust. NGC 4473 has unusual photometric properties that may be related to a merging component (§ 5.6). NGC 4697 has a dust ring that may have been deposited by a merger. As can be seen in Figure 26, all three of these fall reasonably close to the $M_{\rm BH}$-σ relation. Two of these, NGC 4697 and NGC 4473, are among our most secure BH detections.

7. CONCLUSIONS

We have presented long-slit spectroscopy from STIS aboard *HST* and the MDM 2.4 m telescope that is used to derive black hole masses for 10 galaxies by G00. A total of 90% of the galaxies have a centrally peaked velocity dispersion and/or a higher dispersion from STIS than the ground-based Modspec. The galaxies with the strongest rotational support, as quantified by $v_{\rm max}/\sigma_{\rm STIS}$, have the smallest dispersion excess at STIS resolution. When only our 10 galaxies are used for a fit to $M_{\rm BH}$-σ, the slope is 3.68, which is similar to the value of 3.75 found by G00 for 26 galaxies. We review individual galaxies and identify candidates for recent merger: NGC 4697, NGC 3608, and NGC 4473. These galaxies are *not* outliers in the $M_{\rm BH}$-σ relation. We also identify pseudobulges in NGC 3384 and NGC 7457 and find that they also obey the $M_{\rm BH}$-σ relation. Finally, we find a trend toward flat-topped LOSVDs (i.e., negative values of h4) at the center of the galaxies, implying a tangential bias in the stellar velocity dispersion.
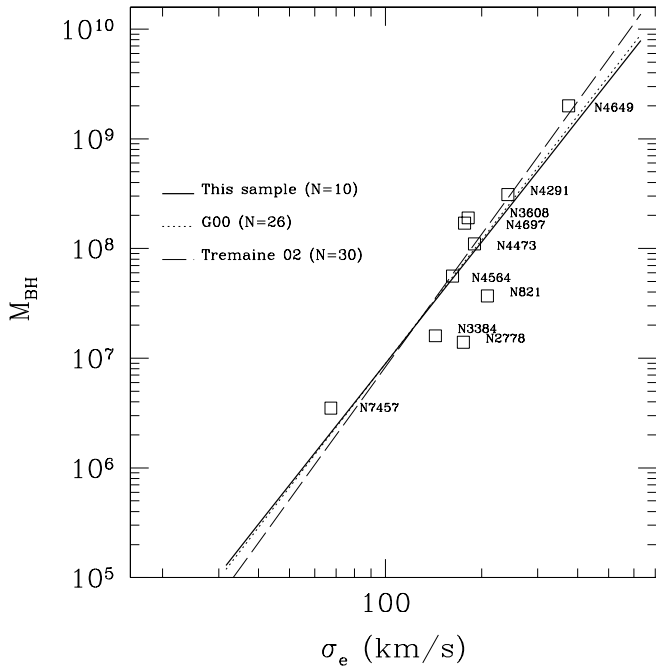
Fig. 26.—Updated plot of $M_{\rm BH}$-σ for only the galaxies in this paper (*labeled squares*). The best-fit line to these 10 galaxies is shown as a solid line. We overlay the original fit by G00 (*dotted line*) and the preferred fit by Tremaine et al. (2002; *dashed line*).

REFERENCES

Andredakis, Y. C., Peletier, R. F., & Balcells, M. 1995, MNRAS, 275, 874
Beers, T. C., Flynn, K., & Gebhardt, K. 1990, AJ, 100, 32
Bender, R. 1988, A&A, 193, L7
———. 1990, A&A, 229, 441
Bender, R., Döbereiner, S., & Möllenhoff, C. 1988, A&AS, 74, 385
Bender, R., Saglia, R. P., & Gerhard, O. E. 1994, MNRAS, 269, 785 (BSG94)
Bertola, F., & Capaccioli, M. 1975, ApJ, 200, 439
Binney, J. J., et al. 1990, ApJ, 361, 78
Bohringer, H., et al. 2000, ApJS, 129, 435
Bower, G. A., et al. 1997, ApJ, 492, L111
———. 2001, ApJ, 550, 75
Bureau, M., et al. 2002, in ASP Conf. Ser. 282, Galaxies: The Third Dimension, ed. M. Rosado, L. Binette, & L. Arias (San Francisco: ASP), 208
Busarello, G., Capaccioli, M., D'Onofrio, M., Longo, G., Richter, G., & Zaggia, S. 1996, A&A, 314, 32
Busarello, G., Longo, G., & Feoli, A. 1992, A&A, 262, 52
Byun, Y.-I., et al. 1996, AJ, 111, 1889
Caon, N., Capaccioli, M., & Rampazzo, R. 1990, A&AS, 86, 429
Cappellari, M., Verolme, E. K., van der Marel, R. P., Kleijn, G. A. V., Illingworth, G. D., Franx, M., Carollo, C. M., & de Zeeuw, P. T. 2002, ApJ, 578, 787
Carollo, C. M., Franx, M., Illingworth, G. D., & Forbes, D. A. 1997, ApJ, 481, 710
Carter, D. 1987, ApJ, 312, 514
Cinzano, P., & van der Marel, R. P. 1994, MNRAS, 270, 325
Cretton, N., & van den Bosch, F. C. 1999, ApJ, 514, 704
Davies, R. L. 1981, MNRAS, 194, 879
Davies, R. L., Efstathiou, G., Fall, S. M., Illingworth, G., & Schechter, P. L. 1983, ApJ, 266, 41
Davoust, E., Lelievre, G., Maury, A., & Nieto, J.-L. 1984, MNRAS, 209, 503
de Bruyne, V., Dejonghe, H., Pizzella, A., Bernardi, M., & Zeilinger, W. W. 2001, ApJ, 546, 903
Dejonghe, H., de Bruyne, V., Vauterin, P., & Zeilinger, W. W. 1996, A&A, 306, 363
de Vaucouleurs, G., de Vaucouleurs, A., Corwin, H. G., Buta, R. J., Paturel, G., & Fouquè, P. 1991, Third Reference Catalogue of Bright Galaxies (New York: Springer) (RC3)
de Zeeuw, P. T., et al. 2002, MNRAS, 329, 513
di Matteo, T., & Fabian, A. C. 1997, MNRAS, 286, 393
Dressler, A., & Richstone, D. 1990, ApJ, 348, 120
Dressler, A., et al. 1987, ApJ, 313, 42
Emsellem, E., Dejonghe, H., & Bacon, R. 1999, MNRAS, 303, 495
Fabbiano, G., & Trinchieri, G. 1987, ApJ, 315, 46
Faber, S. M., & Jackson, R. E. 1976, ApJ, 204, 668
Faber, S. M., et al. 1997, AJ, 114, 1771
Ferrarese, L., Ford, H. C., & Jaffe, W. 1996, ApJ, 470, 444
Ferrarese, L., & Merritt, D. 2000, ApJ, 539, L9
Ferrari, F., Pastoriza, M. G., Macchetto, F., & Caon, N. 1999, A&AS, 136, 269
Fisher, D. 1997, AJ, 113, 950
Fisher, D., Illingworth, G. D., & Franx, M. 1995, ApJ, 438, 539
Forbes, D. A. 1991, MNRAS, 249, 779
Gebhardt, K., et al. 1996, AJ, 112, 105
———. 2000, ApJ, 539, L13 (G00)
———. 2001, AJ, 122, 2469
———. 2003, ApJ, 583, 92
Gerhard, O. E. 1993, MNRAS, 265, 213
González, J. J. 1993, Ph.D. thesis, Univ. California, Santa Cruz
Goudfrooij, P., Hansen, L., Jørgensen, H. E., & Nørgaard-Nielsen, H. U. 1994a, A&AS, 105, 341
Goudfrooij, P., Hansen, L., Jørgensen, H. E., Nørgaard-Nielsen, H. U., de Jong, T., & van den Hoek, L. B. 1994b, A&AS, 104, 179
Halliday, C., Davies, R. L., Kuntschner, H., Birkinshaw, M., Bender, R., Saglia, R. P., & Baggley, G. 2001, MNRAS, 326, 473
Harms, R. J., et al. 1994, ApJ, 435, L35
Ho, L. C., Filippenko, A. V., & Sargent, W. L. W. 1997, ApJS, 112, 315
Hodge, P. E., et al. 1998, in ASP Conf. Ser. 145, Astronomical Data Analysis Software and Systems VII, ed. R. Albrecht, R. N. Hook, & H. A. Bushouse (San Francisco: ASP), 316
Illingworth, G. 1977, ApJ, 218, L43
Isobe, T., Feigelson, E. D., & Nelson, P. I. 1986, ApJ, 306, 490
Jedrzejewski, R. I., & Schechter, P. L. 1988, ApJ, 330, L87
———. 1989, AJ, 98, 147
Joseph, C. L., et al. 2001, ApJ, 550, 668
Jungwiert, B., Combes, F., & Axon, D. J. 1997, A&AS, 125, 479
Kaprolin, W., & Zeilinger, W. W. 2000, A&AS, 145, 71
Kim, D.-W. 1989, ApJ, 346, 653
Koopman, R. A., Kenney, J. D. P., & Young, J. 2001, ApJS, 135, 125
Kormendy, J. 1985, ApJ, 292, L9

Kormendy, J. 1993, in IAU Symp. 153, Galactic Bulges, ed. H. Habing & H. Dejonghe (Dordrecht: Kluwer), 209
Kormendy, J., & Gebhardt, K. 2001, in The 20th Texas Symposium on Relativistic Astrophysics, ed. J. C. Wheeler & H. Martel (New York: AIP), 363
Kormendy, J., & Richstone, D. 1995, ARA&A, 33, 581
Kormendy, J., et al. 2003, ApJ, submitted
Kronawitter, A., Saglia, R. P., Gerhard, O. E., & Bender, R. 2000, A&AS, 144, 53
Lauer, T. R. 1985, MNRAS, 216, 429
Lauer, T. R., et al. 1991, ApJ, 369, L41
———. 1995, AJ, 110, 2622
———. 1996, ApJ, 471, L79
———. 2002, AJ, 124, 1975
Leitherer, C., et al. 2001, STIS Instrument Handbook, Version 5.1 (Baltimore: STScI)
Macchetto, F., Pastoriza, M., Caon, N., Sparks, W. B., Giavalisco, M., Bender, R., & Capaccioli, M. 1996, A&AS, 120, 463
Magorrian, J., et al. 1998, AJ, 115, 2285
Makino, J. 1997, ApJ, 478, 58
Mamon, G. A. 1989, A&A, 219, 98
McElroy, D. B. 1995, ApJS, 100, 105
Merritt, D. 1997, AJ, 114, 228
Michard, R., & Marchal, J. 1994, A&AS, 105, 481
Milosavljević, M., & Merritt, D. 2001, ApJ, 563, 34
Morton, D. C., & Chevalier, R. A. 1973, ApJ, 179, 55
Nieto, J.-L., Bender, R., Arnaud, J., & Surma, P. 1991, A&A, 244, L25
Nieto, J.-L., Capaccioli, M., & Held, E. V. 1988, A&A, 195, L1
Nieto, J.-L., Poulain, P., & Davoust, E. 1994, A&A, 283, 1
Peletier, R. F. 1989, Ph.D. thesis, Univ. Groningen
Peletier, R. F., Davies, R. L., Illingworth, G. D., & Davis, L. E. 1990, AJ, 100, 1091
Pellegrini, S. 1999, A&A, 351, 487
Pence, W. 1998, in ASP Conf. Ser. 145, Astronomical Data Analysis Software and Systems VII, ed. R. Albrecht, R. N. Hook, & H. A. Bushouse (San Francisco: ASP), 97
Press, W. H., Teukolsky, S. A., Vetterling, W. T., & Flannery, B. P. 1992, Numerical Recipes in FORTRAN: The Art of Scientific Computing (2d ed.; Cambridge: Cambridge Univ. Press)
Prugniel, Ph., Zasov, A., Busarello, G., & Simien, F. 1998, A&AS, 127, 117
Ravindranath, S., Ho, L. C., Peng, C. Y., Filippenko, A. V., & Sargent, W. L. W. 2001, AJ, 122, 653
Rest, A., et al. 2001, AJ, 121, 2431
Richstone, D., et al. 1998, Nature, 395, A14
Rix, H.-W., de Zeeuw, P. T., Cretton, N., van der Marel, R. P., & Carollo, C. M. 1997, ApJ, 488, 702
Roberts, M. S., Hogg, D. E., Bregman, J. N., Forman, W. R., & Jones, C. 1991, ApJS, 75, 751
Rood, H. J., & Williams, B. A. 1985, ApJ, 288, 535
Saglia, R. P., Kronawitter, A., Gerhard, O., & Bender, R. 2000, AJ, 119, 153
Saha, P., & Williams, T. B. 1994, AJ, 107, 1295
Sahu, D. K., Pandey, S. K., & Kembhavi, A. K. 1996, Bull. Astron. Soc. India, 24, 777
Sandage, A., & Bedke, J. 1994, The Carnegie Atlas of Galaxies (Washington: Carnegie Inst.)
Sandage, A., & Tammann, G. A. 1980, A Revised Shapley-Ames Catalog of Bright Galaxies (Washington, DC: Carnegie Institution)
Schneider, S. 1985, ApJ, 288, L33
Sil'Chenko, O. K. 1997, AZh, 74, 643
Singh, K. P., Prabhu, T. P., Kembhavi, A. K., & Bhat, P. N. 1994, ApJ, 424, 638
Sofue, Y., & Wakamatsu, K.-I. 1993, PASJ, 45, 529
Stanger, V., & Warwick, R. S. 1986, MNRAS, 220, 363
Tomita, A., Aoki, K., Watanabe, M., Takata, T., & Ichikawa, S.-I. 2000, AJ, 120, 123
Tonry, J. L., Dressler, A., Blakeslee, J. P., Ajhar, E. A., Fletcher, A. B., Luppino, G. A., Metzger, M. R., & Moore, C. B. 2001, ApJ, 546, 681
Trager, S. C., Faber, S. M., Worthey, G., & González, J. J. 2000, AJ, 119, 1645
Tremaine, S., et al. 2002, ApJ, 574, 740
Trinchieri, G., & di Serego Alighieri, S. 1991, AJ, 101, 1647
van den Bosch, F. C., Ferrarese, L., Jaffe, W., Ford, H. C., & O'Connell, R. W. 1994, AJ, 108, 1579
van der Marel, R. P. 1994a, ApJ, 432, L91
———. 1994b, MNRAS, 270, 271
van der Marel, R. P., & Franx, M. 1993, ApJ, 407, 525
van der Marel, R. P., & van den Bosch, F. C. 1998, AJ, 116, 2220
Veron-Cetty, M.-P., & Veron, P. 1988, A&A, 204, 28
Wrobel, J. M., & Heeschen, D. S. 1991, AJ, 101, 148
Wrobel, J. M., & Herrnstein, J. R. 2000, ApJ, 533, L111
Young, P., Sargent, W. L. W., Boksenberg, A., Lynds, C. R., & Hartwick, F. D. A. 1978, ApJ, 222, 450